Chair of Functional Materials and Materials Systems
Department of Materials Science

Doctoral Thesis

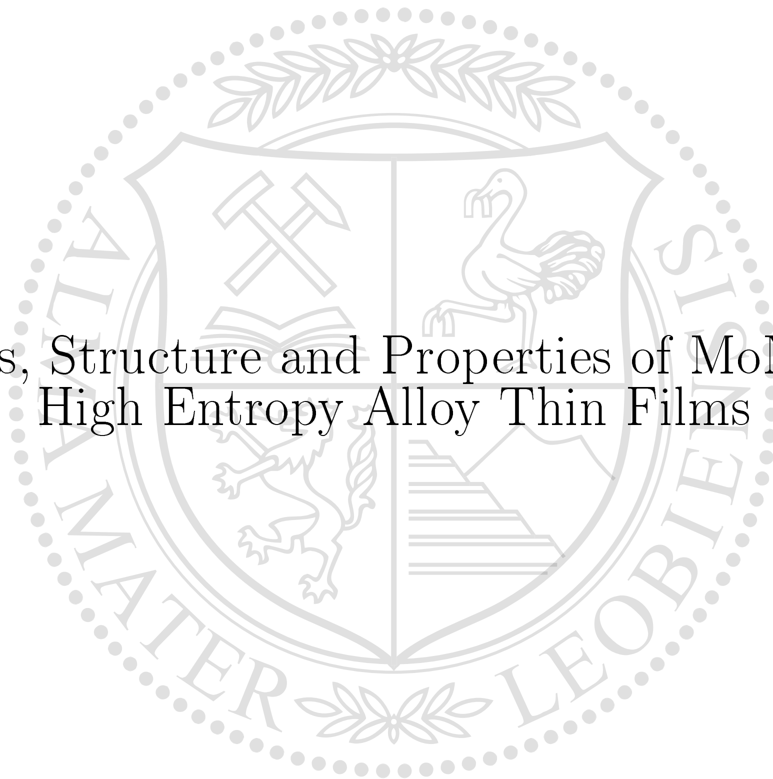

Synthesis, Structure and Properties of MoNbTaVW High Entropy Alloy Thin Films

Ao Xia

June 2020

This thesis was supported by the Austrian Science Fund (FWF, Project No. I2484-N36) at the Department of Materials Science at Montanuniversität Leoben, Austria, in cooperation with the Department of Solid State Sciences at Ghent University, Belgium.

EIDESSTATTLICHE ERKLÄRUNG

Ich erkläre an Eides statt, dass ich diese Arbeit selbständig verfasst, andere als die angegebenen Quellen und Hilfsmittel nicht benutzt, und mich auch sonst keiner unerlaubten Hilfsmittel bedient habe.

Ich erkläre, dass ich die Richtlinien des Senats der Montanuniversität Leoben zu "Gute wissenschaftliche Praxis" gelesen, verstanden und befolgt habe.

Weiters erkläre ich, dass die elektronische und gedruckte Version der eingereichten wissenschaftlichen Abschlussarbeit formal und inhaltlich identisch sind.

Datum 30.06.2020

Unterschrift Verfasser/in
Ao, Xia

Acknowledgement

I would like to thank Dr. Robert Franz for giving me the opportunity to carry out the present work within his research group, guiding my academic path since my Master's thesis and having trust in my initiatives.

I would like to express my special gratitude and thanks to Prof. Christian Mitterer for hosting me in his lab. The constructive, fruitful and motivating discussions over the recent years vastly contributed to my academic experience and the development of personality.

I gratefully acknowledge the support of the Austrian Science Fund, which gave us the opportunity to closely collaborate with Prof. Diederik Depla and Robin Dedoncker from Ghent University.

I am very grateful to Dr. Megan J. Cordill, Dr. Oleksandr Glushko, Sabrina Hirn, Karl-Heinz Pichler, Velislava Terziyska, Thomas Lukas, Alexander Wenda, Alessandro Togni, Isabella Eichbauer and Patrice Kreiml for their dedicated contribution and support to the current thesis.

At this point, I would like to appreciate the help of my colleagues at the Montanuniversität Leoben，in particular I want to express my gratitude towards the Chair of Functional Materials for the past, current and future support.

最后我要感谢我的父母常年对我的支持和理解。他们默默地奉献是我求学和成人的支持和动力。感谢他们为我们一代所付出一辈子的辛劳，感谢我的弟弟和妹妹，感谢我的朋友和亲人。

Contents

1 Introduction **1**

2 High entropy alloys **5**

2.1 Terminology . . . 5
2.2 Motivations and definitions . . . 6
2.2.1 Composition-based definition . . . 7
2.2.2 Entropy-based definition . . . 7
2.2.3 Four HEA core effects . . . 8
2.3 Taxonomy . . . 11
2.3.1 Major alloy families . . . 12
2.3.2 HEA thin films: Applications and potential . . . 14

3 Coating synthesis **17**

3.1 Electrical discharges . . . 17
3.2 Sputter deposition . . . 19
3.2.1 Physical basics . . . 19
3.2.2 Magnetron sputter deposition . . . 19
3.3 Cathodic arc deposition . . . 22
3.3.1 Plasma generation: Cathode spot . . . 23
3.3.2 Macroparticles . . . 24
3.3.3 Arc source design and magnetic fields . . . 25

4 Methods **31**

5 Results and discussion **33**

5.1 Angular-dependent deposition . . . 33
5.1.1 Deposition rate . . . 33
5.1.2 Chemical composition . . . 34
5.1.3 Morphology . . . 35
5.1.4 Structure . . . 35
5.1.5 Mechanical properties . . . 38

5.1.6 Discussion 42
5.2 Thermal stability 46
5.3 Effect of N incorporation 52
5.3.1 Chemical composition and structure 52
5.3.2 Electrical and mechanical properties 54
5.3.3 Discussion 54
5.4 Electromechanical properties 60
5.4.1 Metallic thin films 60
5.4.2 Nitride thin films 64
5.4.3 Discussion 68

6 Conclusions **71**

7 Abbreviations **73**

1 Introduction

Ever since the beginning of human civilization, improvements in materials were first achieved by modifying materials available in the living environment (stones, woods, bones, etc.). However, due to the inconsistent characteristics of organic materials, some of the tooling materials were replaced by metals soon after their discovery. Significant enhancements in material properties were enabled by alloying a base element with promising mechanical properties with fractions of other elements. Bronze, e.g., was a result of alloying elemental Cu with a small amount of Sn. This progress in material processing marked the beginning of the bronze age allowing the first ancient civilizations to experience massive achievements in culture and technology. During the bronze age, a demand for protective and decorative thin films for the expensive base material arose and, hence, copper or bronze statues and religious artefacts were gilded for the first time [1]. Followed by the progress in carbon control to make steel (iron alloys), the frontiers of materials science were pushed further during the iron age and refined until the middle age. During the medieval period, cultural, political and economic exchanges between ancient China, the Byzantine Empire, the Islamic world and Western Europe contributed to the foundation for modern science and the steady development in metallurgy and materials science allowed the discovery of new elements and enhancement of material properties. Even though the strive for better materials forced humanity to advance in material design and production, development of new materials nowadays has become challenging [2]. Conventional alloy concepts are based on one major base element, which is diluted with alloying elements to improve the material properties of the alloy family. However, the demand for alloys with outstanding high temperature, mechanical, diffusion and corrosion properties is difficult to meet with the currently available stable alloy families, e.g., Fe, Al, Mg or Ni based alloys. Therefore, new alloying strategies should be considered to discover materials with advanced properties.

In recent years, a novel class of alloys derived from the multi-principal element design concept has attracted increasing attention. High entropy alloys (HEAs) are a new class of materials, first introduced independently by Yeh and Cantor in 2004, featuring outstanding physical and chemical properties [3, 4]. The initial goal of HEAs was to enhance the material properties by avoiding the formation of complicated and brittle intermetallic phases. Instead of alloying a base element with minor fractions of different elements, the alloying strategy

of HEAs is based on the intermixing of 5 or more elements in near equiatomic ratios. It is believed that the increase in entropy of mixing can explain the stabilization of single-phase, solid solution metallic alloys rather than the formation of intermetallic or other complex phases. HEAs are reported to exhibit high hardness, good wear resistance, good corrosion properties, limited diffusion kinetics, high temperature strength and high thermal stability [3, 5–8]. The obtained material properties show potential for a wide range of future applications. While there is already extensive literature available for bulk HEAs, thin film HEAs are still relatively unexplored.

Thin films greatly enhance the properties of a material by combining a coating with the respective substrate material. This enables surface properties of materials technically and economically unreachable by traditional bulk materials. By controlling the deposition process, e.g. hard coatings deposited on bulk materials are engineered to the desired requirements such as strength, hardness, thermal diffusion, oxidation resistance and fracture toughness [9]. Traditionally, coatings are applied to optical, electronic and magnetic, tooling and machining applications as well as to decorative purposes. The first applied hard coatings for cutting applications were binary nitrides and carbides, e.g. TiN, TiC and CrN followed by diamond or diamond-like carbon coatings. Further improvements in mechanical properties and oxidation resistance have been achieved by, e.g., ternary nitrides such as TiAlN and CrAlN [10].

The aim of the present work is to contribute to the understanding of HEA thin films by collecting fundamental experimental work focused on the relations between synthesis, structure and properties of these films. Therefore, MoNbTaVW HEA thin films were synthesized on various substrates utilizing different physical vapor deposition (PVD) methodes, namely direct current (dc) magnetron sputter deposition (MSD), high power impulse magnetron sputtering (HiPIMS) and cathodic arc deposition (CAD) . The influence of different growth conditions such as the deposition angle on structure and properties of the thin films was studied. Further, vacuum annealing of MoNbTaVW thin films was conducted to evaluate their thermal stability as well as their mechanical and electrical properties after annealing. The effect of N on HEA thin films was investigated by synthesizing MoNbTaVW thin films in N containing atmosphere using CAD and MSD. In-situ tensile straining tests were conducted to investigate the electromechanical properties of metallic and nitride MoNbTaVW HEA thin films deposited on flexible polymimide (PI) substrates.

The outline of the thesis starts with a general overview of HEAs regarding definition, characterization, design strategy and possible applications by reviewing recently published literature. In the next chapter, selected PVD methods for the synthesis of HEA thin films are

described. The obtained experimental results are disclosed in Chapter 5 and discussed based on the current state of the art available in literature. Finally, a summary of the obtained results is given in order to point out the interrelationship between synthesis, structure and properties of HEAs.

2 High entropy alloys

In the late eighteenth century, German scientist Franz Karl Achard first studied multi-principal element alloys (MPEAs) with five to seven elements in equimass composition [11]. He mixed together the most common elements at his time, including Fe, Cu, Pb, Sn, Zn, Bi, Sb and As. The properties of the alloys differed from the base elements but were not alluring. This was the reason why MPEAs were not further investigated at the time. However, it is therefore believed that Franz Karl Achard was the first metallurgist to study this new alloying concept and, hence, he was the predecessor for the works of Jien-Wei Yeh and Brian Cantor on HEAs and multi-component alloys, respectively.

2.1 Terminology

According to Miracle and Senkov, different approaches accompanied by new names for this new class of materials cause controversy and confusion in the community, which distracts from the major objective of exploring the vast number of alloys proposed by this alloying strategy [12]. Alternative terms including MPEA, complex concentrated alloys (CCA) and baseless alloys were introduced by Miracle and depicted in Figure 2.1 to describe the vast area of multi-element alloys. MPEA is the umbrella term for all multi-component alloys including concentrated ternary and quaternary alloys as well as CCAs and other alloys that may not fit the HEA definitions but nevertheless contribute to the study or development of MPEAs. HEAs are referred to as alloys when the configurational entropy or the intend to produce single-phase solid solution microstructures are of importance, whereas multi-phase microstructures are included in the CCA concept.

The entropy-based definition only focuses on the configurational entropy. While vibrational, electronic and magnetic terms are acknowledged, the configurational term is claimed to dominate in earlier studies [13]. However, more recent studies show that the impact of vibrational entropy is much larger, but the thermodynamic competition between solid solution and intermetallic phases is rather complicated and much of the vibrational entropy cancels in parent and product phases [12].

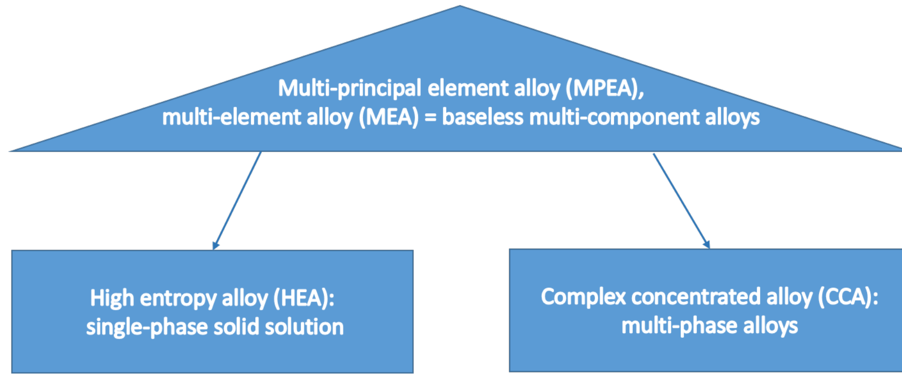

Figure 2.1: Different terminologies for multi-principle element alloys.

2.2 Motivations and definitions

At the turn of the millennium, independent investigations led by Brian Cantor and Jien-Wei Yeh abandoned traditional alloying concepts focusing on one base element and adopted the equiatomic multi-component alloying strategy. The motivation for multi-component alloys proposed by Cantor is to investigate the unexplored central region of multi-component alloy phase space [14]. However, in contrast to multi-component alloys, the HEA definition by Yeh intends to find single-phase solid solution alloys containing at least five principal elements, each with a fraction between 5 and 35 at.% [3].

The Gibbs free energy of mixing is the established criterion to predict thermodynamically stable phases by minimizing the ΔG_{mix}:

$$\Delta G_{\text{mix}} = \Delta H_{\text{mix}} - T\Delta S_{\text{mix}} \tag{2.1}$$

where ΔH_{mix} is the mixing enthalpy, T the temperature and ΔS_{mix} the mixing entropy. The total mixing entropy consists of the dominant configurational entropy, and less contributing vibrational entropy, magnetic dipole and electronic randomness. For simplification, the latter three contributions are neglected and, hence, the mixing entropy equals the configurational entropy. The Gibbs free energy for all competing phases must be estimated and the phase or the phases with the lowest G predict the stable microstructure of that alloy. Although existing physical metallurgy knowledge suggests that such multi-component alloys may develop intermetallic compounds and, therefore, give rise to complex and brittle microstructures, HEAs tend to form solid solution phases with simple structures, such as body-centered cubic (bcc) or face-centered cubic (fcc) structures. According to Yeh et al. [3], this is attributed to their high ΔS_{mix}. This implies that a high mixing entropy enhances the mutual solubility among elements and prevents phase separation into terminal solution

phases or intermetallic compounds. Correspondingly, solid solution phases become highly competitive for the equilibrium state and more stable especially at high temperatures [15]. The results were single-phase solid solutions with improved mechanical properties of these bulk alloys. Therefore, two definitions of HEAs are given in the following sections.

2.2.1 Composition-based definition

In the earliest paper [3], HEAs are defined as an alloy with a composition containing 5 to 13 principal elements with the concentration of each element being between 5 and 35 at.%. However, HEAs may not be equiatomic and even contain minor fractions of elements to modify the properties of the base HEA which further increases the number of HEAs [15]. This composition-based definition places no boundaries on the magnitude of entropy and the presence of a single-phase solid solution [5].

2.2.2 Entropy-based definition

HEA studies fueled by the entropy-based definition appear to be motivated by the concept of high configurational entropy favoring the formation of single-phase solid solution phases over alloys with intermetallic phases [3, 12]. The Boltzmann equation gives a simple approach to calculate the relationship between the configurational entropy change per mole ΔS_{conf} in an ideal solid solution and the complexity of a system:

$$\Delta S_{\mathrm{conf}} = -k \ln w = R(\frac{1}{n}\ln\frac{1}{n} + \frac{1}{n}\ln\frac{1}{n} + ... + \frac{1}{n}\ln\frac{1}{n}) = -R \ln \frac{1}{n} = R \ln n \qquad (2.2)$$

There, k is Boltzmann's constant, w is the number of ways of mixing, R is the gas constant (8.314 J/K mol) and n is the number of elements. Table 2.1 lists the configurational entropies, calculated using Equation 2.2, of equiatomic alloys as a function of n. If the number of elements in equiatomic ratios is sufficiently high, the ΔS_{conf}, mainly influencing the ΔS_{mix}, increases, which means that the mixing entropy of the solid solution phases prevail over the mixing enthalpy of the intermetallic compounds [5]. Based on this view, the alloy world can be categorized according to the configurational entropies, as schematically shown in Figure 2.2. Steels are examples for low ($\Delta S_{\mathrm{conf}} < 0.69$R), while bulk metallic glasses, Ni and Co-base superalloys are medium ($0.69\mathrm{R} < \Delta S_{\mathrm{conf}} < 1.61\mathrm{R}$) and for ΔS_{conf} > 1.61R a new alloy class called HEAs may be established. Although the configurational entropy is dominant over the other three contributions, it requires that atoms occupy random lattice positions which rarely occurs in metallic solutions. This definition also implies that

Table 2.1: Configurational entropies of equiatomic alloys with up to 13 constituent elements (after [5]).

n	1	2	3	4	5	6	7	8	9	10	11	12	13
$\Delta S_{\mathrm{conf}}/R$	0	0.69	1.1	1.39	1.61	1.79	1.95	2.08	2.2	2.3	2.4	2.49	2.57

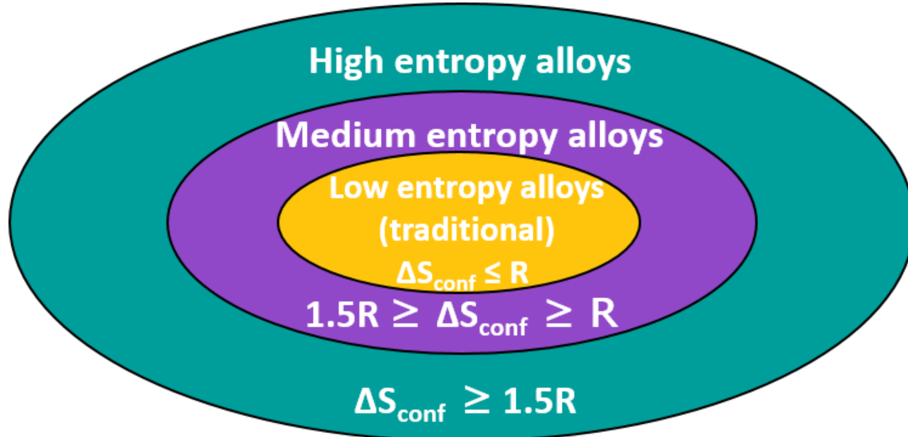

Figure 2.2: Alloy world based on the configurational entropy (after [5]).

an alloy's entropy is unaffected by temperature. The temperature effect can be mild, by causing small changes in short-range atomic ordering, or it can be dramatic, by chemical partitioning between parent and product phases at a first order transformation. To address these issues, the entropy-based definition assumes the alloy can be represented by the liquid solution and high-temperature solid solution states, where the thermal energy is sufficiently high to cause different elements to have random positions in the structure. This characterizes an alloy by the maximum entropy possible, and implies that such a state is achieved at high temperature or in the liquid state. However, even binary metallic liquids typically do not have random atomic positions at the melting temperature [12].

2.2.3 Four HEA core effects

In early publications four core effects are often used to describe HEAs: the high entropy effect for thermodynamics, the sluggish diffusion effect for kinetics, the lattice distortion effect for structure and properties and the cocktail effect. The first three are hypotheses and the cocktail effect is a separate characterization of HEAs. These core effects have been debated since they were published. However, they illustrate some fundamental aspects of HEAs in a comprehensible way.

The high entropy effect

As the name implies, the high entropy effect is the signature concept of HEAs and proposes that with increasing configurational entropy in near-equiatomic alloys with 5 or more elements the formation of solid solution phases is favored over competing intermetallic compounds. Three possible categories of competing states are known for the solid state of an alloy, i.e. elemental phases, solid solution phases and intermetallic compounds. Elemental phases are defined as a solid solution, based on one pure metal element. Solid solutions are phases with the complete mixing of all elements in the structure of typically hexagonal close-packed (hcp), bcc or fcc structure, as depicted in Figure 2.3. Intermetallic compounds are stoichiometric compounds composed of specific superlattices such as NiAl with B2 structure or Ni_3Ti with $D0_{24}$ structure [5]. Although non-stoichiometric intermetallic phases are in a broader sense another type of solid solution, they should not be considered as HEAs [12]. To support the high entropy effect, the idealized configurational entropy is compared with the entropy of fusion for pure metals or with the formation enthalpies of selected intermetallic compounds. Comparisons are generally qualitative (characterizing enthalpies and entropies as "high" or "low"), and are applied broadly by comparing all solid solution phases to all intermetallic compounds, without considering specific systems and without acknowledging that a wide range of stabilities exists in solid solution and intermetallic phases. According to the second law of thermodynamics, the state having the lowest Gibbs free energy of mixing, ΔG_{mix}, among all possible states would be the equilibrium state. To elucidate a high entropy effect in enhancing the formation of solid solution phases and inhibiting the formation of intermetallic compounds, HEAs composed of constituting elements with stronger bonding energies between each other are considered. Elemental phases based on one major element have small ΔH_{mix} and ΔS_{mix}, compound phases have large ΔH_{mix} but small ΔS_{mix}, while, solid solution phases containing multiple elements have medium ΔH_{mix} and high ΔS_{mix}. As a result of the increasing contribution of the $-T\Delta S_{\mathrm{mix}}$ term, solid solution phases become highly competitive for equilibrium state and more stable especially at high temperatures. This implies that the high mixing entropy enhances the mutual solubility among elements and prevents phase separation into terminal solid solution phases or intermetallic compounds [15].

The lattice distortion effect

Severe lattice distortion comes from the different atom sizes of the multi-element matrix [15]. The lattice strain and stress are mainly caused by atomic size mismatches of random element

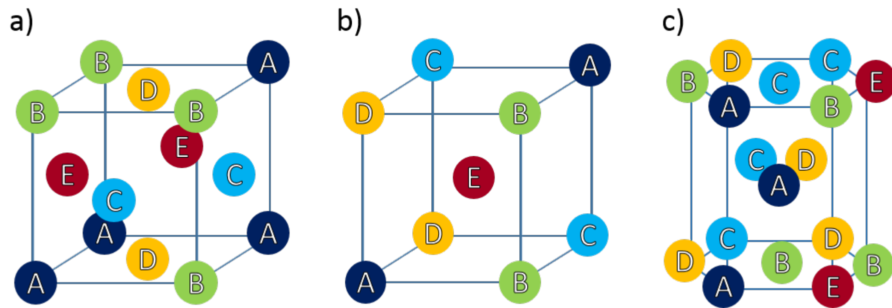

Figure 2.3: Disordered arrangement of A, B, C, D and E atoms in the a) fcc, b) bcc and c) hcp crystall lattice [12].

occupation in the crystal as shown in Figure 2.4 [16]. These distortions are claimed to be more severe than in conventional alloys based on one major element due to different bonding energy and crystal structure tendency among constituting elements. In conventional alloys, most matrix atoms have repeating neighboring atoms. Uncertainty in atom positions from these distortions contributes to the excess configurational entropy, and is claimed to decrease the intensity of X-ray diffraction (XRD) peaks, to increase hardness, to reduce electrical and thermal conductivity and to reduce the temperature dependence of these properties. These claims seem physically sensible, but systematic attempts to quantify most of these effects and to separate them from other contributions are still missing. For example, the shear modulus mismatch between constituting atoms may also contribute to hardening, and electrical and thermal conductivities can be influenced by the electronic structures associated with variations in local bond states [12].

The sluggish diffusion effect

The formation of new phases is explained by cooperative diffusion of many different kinds of atoms. In HEAs, diffusion is dominated by substitutional diffusion characterized by significant higher activation energies. This claim is based on secondary observations that include formation of nanocrystals and amorphous phases upon solidification and on qualitative interpretations of microstructural stability upon cooling. Appearance of nanocrystals in as-cast $Al_xCoCrCuFeNi$ and retention of nanocrystals in AlCrMoSiTi after annealing were interpreted to signify slow diffusion [12]. Furnace cooling of $Al_{0.5}CoCrCuFeNi$ avoids the formation of low-temperature phases, and AlMoNbSiTaTiVZr is a better diffusion barrier than TaN/TiN or Ru/TaN - both of these results have been used to support the sluggish diffusion hypothesis [12]. Tsai stated that the higher activation energies in HEAs are attributed to the larger lattice potential energy (LPE) fluctuations [17]. Since atoms tend to minimize

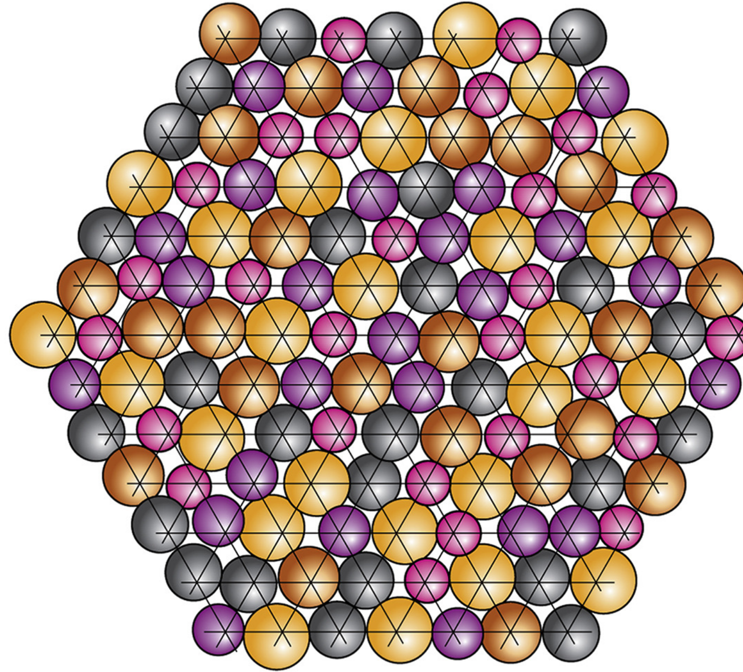

Figure 2.4: Severe lattice distortion in a multi-element crystal structure [5].

their energies, lattice sites with lower LPE for an element would become atomic traps and increase the energy barrier and the activation energy for diffusion. As shown in Figure 2.5, two adjacent sites L and M of pure metals would be the same, since configurations around any atom are identical. Thus, the energy barrier (E_{b}) for a migration from L to M equals that from M to L [17]. However, for alloys, the LPE of the two sites will differ by the mean difference (MD). MD describes the average LPE change during atomic migration in a matrix. Thus, the energy barriers for the two opposite atomic jumps are different, and the transition frequencies between L and M are asymmetric. This means, atoms will prefer to stay at lattice sites with lower LPE. Even if an atom jumps into a high-LPE site, the atom will tend to hop back to its previous site. Therefore, the low-LPE sites serve as atomic traps that hinder diffusion. However, data are still limited and wider datasets are needed to better explore the hypothesis that diffusion may be unusually slow in HEAs as a class of materials.

The cocktail effect

The metaphoric term cocktail effect was initially used by Ranganathan to describe "a pleasant, enjoyable mixture" where the end result is unpredicted but greater than the basic ingredients [18]. For example, the addition of light elements, such as Al, can decrease the density of HEAs while the addition of refractory elements such as Nb, can increase the high temperature properties [16]. Differently to the other "core effects", the "cocktail effect" is not

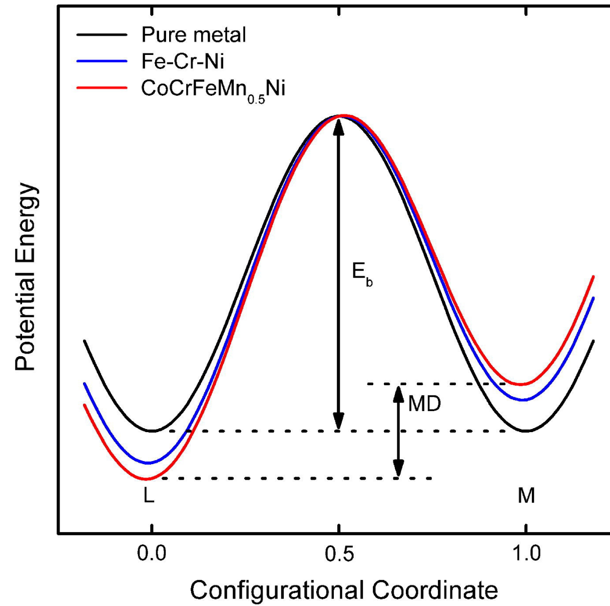

Figure 2.5: Schematic diagram of the variation of LPE and MD during the migration of a Ni atom in different matrices. The MD for pure metals is zero, whereas that for HEAs is the largest [17].

a hypothesis, hence requires no proof. Similar to the name giving mixed drink, the "cocktail effect" rather describes the unexpected exceptional material properties given by the synergies of 5 or more constituting elements. Material properties derived from the unpredictable synergetic effects include physical properties such as a low thermal expansion coefficient, functional properties such as the thermo-electric response or photo-voltaic conversion, and combining mechanical properties such as ultra-high strength with good fracture toughness, fatigue resistance or ductility. However, these properties depend on the material's composition, microstructure, electronic structure and other features in complicated and sensitive ways. Therefore, suitable composition and processing should already be considered in the early materials selection stage to satisfy the desired material properties [19, 20]. For example, bulk refractory MoNbTaW and MoNbTaVW HEAs developed by Senkov et al. have achieved higher melting points with much higher yield strength at elevated temperature than conventional Ni-base and C-base superalloys [21, 22].

2.3 Taxonomy

This section describes the extent of compositions which thus far has been explored and categorized by Miracle and Senkov [12]. The combination of different compositions allows HEAs to form a vast number of new alloy systems with unique combination of elements.

The number of possible HEA systems is:

$$C\binom{n}{r} = \frac{n!}{r!(n-r)!} \tag{2.3}$$

There, r is the amount of principal alloy elements selected from the total number of possible alloying elements n=75. Elements to be considered include stable elements which are not toxic, radioactive or noble gases. This gives over 219 million new HEA systems with $3 \leq r \leq 6$ principal elements. HEAs are summarized in common groups according to the frequency of the elements. Seven distinct HEA families have been identified from a wide range of compositions and are listed in the following subsection 2.3.1. Throughout the thesis, elements within a single alloy are listed in alphabetic order rather than according to their atomic mass. This simple approach for data reporting was proposed by Miracle and Senkov [12]. Thus, MoNbTaVW is reported rather than VNbMoTaW.

2.3.1 Major alloy families

HEAs can be classified into seven alloy families depicted in Figures 2.6 a) and b), which are: 3d transition metal HEAs, refractory metal HEAs, light metal HEAs, lanthanide (4f) transistion metal HEAs, HEA brasses and bronzes, precious metal HEAs and interstitial compound (boride, carbide and nitride) HEAs [12].

3d transition metal HEAs

The oldest and by far most widely studied alloy family contains at least 4 of the 9 following elements: Al, Co, Cr, Cu, Fe, Mn, Ni, Ti and V. 5 of these 9 elements are reported in the alloy CoCrFeMnNi, the so-called "Cantor alloy", first reported in 2004 [14]. Despite being one of the first HEAs reported, this is also a single-phase disordered solid solution alloy. Alloys in the 3d transition metal family are described as extensions of stainless steels and superalloys. About 96% of the 3d transition metal HEAs use Fe, while about 29% of the HEAs in this family contain Mn and only 15% use V as principal elements. Austenitic (fcc), duplex (fcc + bcc) and precipitation hardening stainless steels all have Fe-Cr-Ni as principal elements. Mn is a principal element in some austenitic stainless steels, while compound forming elements such as Al, Cu, Nb and Ti are added in small amounts to precipitation hardened stainless steels. Austenitic nickel alloys have Ni-Cr-Fe or Ni-Cr-Mo as principal elements, with additions of Co, Fe or Mo and smaller additions of Al, Ni or Ti. Nickel superalloys are HEAs based on Ni-Cr-Co-Fe-Mo with sufficient Al, Nb or Ti to form a significant volume fraction of the Ni_3(Al,Nb,Ti) intermetallic phase. Other elements can also

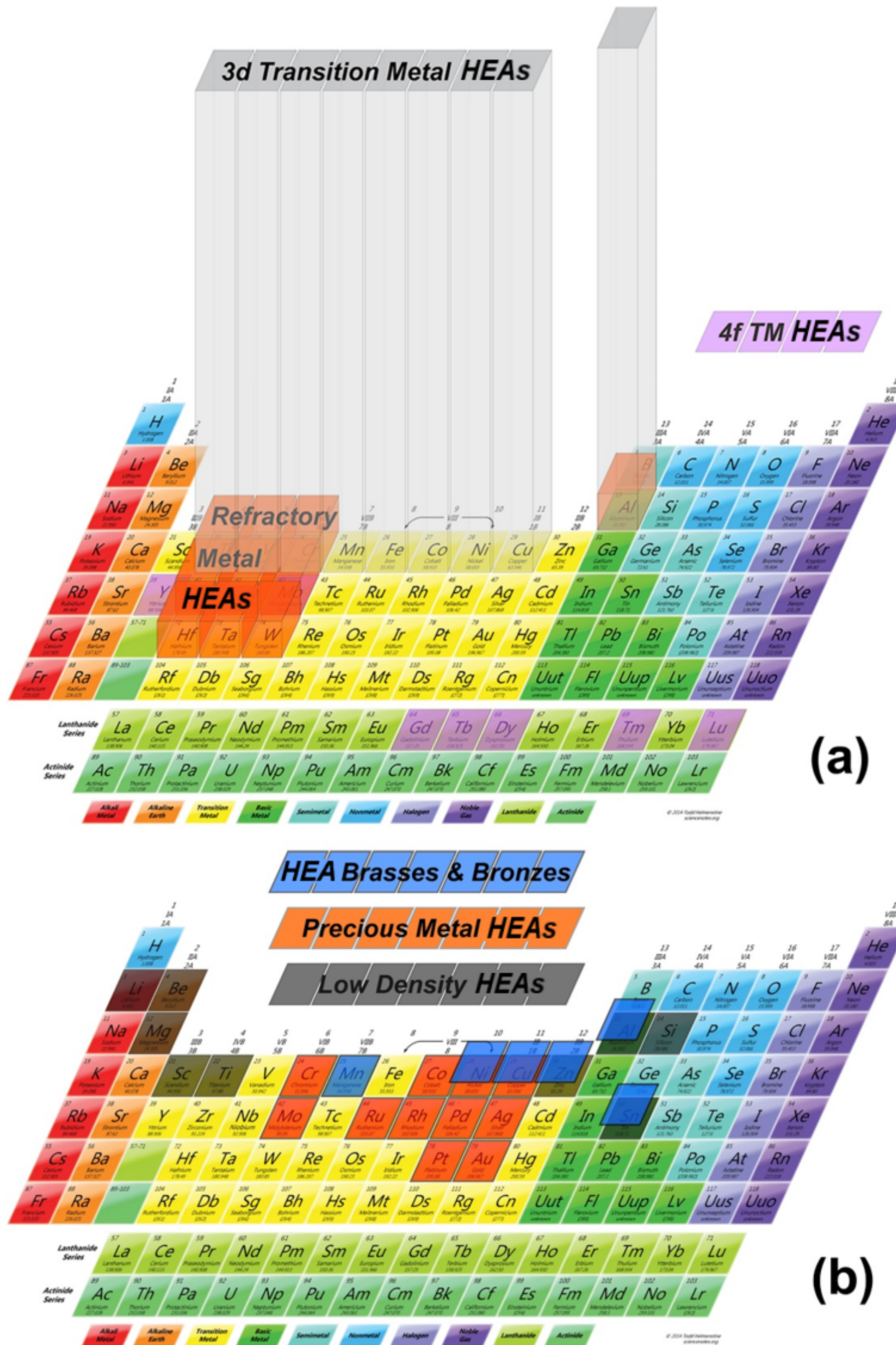

Figure 2.6: Six of the seven HEA families illustrated by element groupings. a) 3d transition metal HEAs, refractory metal HEAs and lanthanide (4f) transition metal HEAs. b) light metal (low density) HEAs, as well as precious metal HEAs and HEA brasses and bronzes. The heights of the boxes in a) are proportional to the number of alloys reported in the two major families [12].

be added to this group as principal elements or as minor additions. The element groupings AlCrFeNi, CoCrFeNi, AlCoFeNi, AlCoCrNi and AlCoCrFe are the most common, and each of these occur in over half of the transition metal HEAs [12].

Refractory metal HEAs

The refractory metal HEA family consists of alloys containing at least 1 of the 5 refractory metals, i.e., Nb, Mo, Ta, W and Re. However, the latter elements are often combined with elements of the wider definition of refractory metals including: Cr, Hf, Ti, V and Zr [12]. This family is much younger and therefore studied much less frequently than the 3d transition metal family of alloys. They are often based on MoNbTaW, HfNbTaZr, CrMoNbTa or CrNbVZr as element groups. The alloys are also mixed with non-refractory elements such as Al or Si to decrease the alloy density and improve the properties. No studies on other refractory elements (Ir, Os, Re, Rh, Ru) have been conducted to date in refractory metal HEAs although they offer new possibilities [12]. Refractory metal HEAs were motivated by the objective to develop new high temperature structural metals. The refractory palette offers very wide ranges in elemental properties such as melting temperature, T_m, (2128-3695 K), density (4.5-19.4 g/cm^3) and elastic moduli (68-411 GPa for Young's modulus). This enhances the flexibility in tuning alloys to achieve a particular property. For example, refractory metal HEAs with low density may favor Cr, Nb, V and Zr, while alloys with Mo, Nb, Ta and W may give the highest T_m. Both, the high T_m and the difference in T_m between elements give unique challenges in producing refractory metal HEAs.

Other alloy families

The idea to create entirely new alloy families came with the introduction of refractory metal HEAs in 2010. The light alloy HEA family is motivated by the development of light structural materials with low density for aerospace and transportation applications. This alloy family is based on elements such as Al, Be, Li, Mg, Sc, Si, Sn, Ti and Zn. However, the broad range of elemental melting and boiling points in this family increases the processing difficulty [12].

The fourth family of alloys contains elements of the lanthanide (4f) elements Dy, Gd, Lu, Tb and Tm, plus the element Y and seeks to discover single-phase solid solution HEAs with a hcp crystal structure. The two alloys in this family reported are DyGdLuTbY and DyGdLuTbTm.

The motivation behind brass and bronze HEAs is to expand the already broad range of brasses and bronzes to achieve higher levels of strength via solid solutions. The alloys use the equi-atomic alloy substitution method based on Al, Cu, Mn, Sn and Zn.

Precious metal HEAs are studied for catalysis applications. These alloys contain at least 4 elements out of Ag, Au, Co, Cr, Cu, Ni, Pd, Pt, Rh and Ru. One example is the single phase hcp MoPdRhRu alloy.

HEAs containing interstitial B, C, N or O are mainly based on alloys from the 3d transition metal or refractory metal HEA families. Most of the alloys contain N with only limited reports on alloys containing C or B. These thin film HEAs are mainly synthesized by reactive gas thin film deposition containing N or O.

2.3.2 HEA thin films: Applications and potential

Surface coatings are widely applied to improve the performance, durability and functionality for cutting, forming and casting applications and components. Similarly, superior chemical resistance is a requirement for coatings used in corrosive environments. Since the 1970s, binary transition metal nitrides, such as TiN, have been widely used to provide wear protection to component surfaces in many industrial applications because of their excellent mechanical properties and corrosion resistance [23]. It has been demonstrated that alloying appropriate elements into a binary nitride coating is an effective way to modify the coating properties. The addition of Cr or Zr to form ternary systems such as $Ti_{1-x}Cr_xN$ or $Ti_{1-x}Zr_xN$ was found to enhance its performance and capability [23]. However, most studies on coatings are still limited to ternary or quaternary systems.

Modern requirements for surface coatings also include better diffusion barrier, biomedical, antibacterial, electromagnetic interference shielding, anti-fingerprint, non-stickiness, and hydrophilic/hydrophobic properties. The excellent properties of HEA thin films such as high strength, ductility, hardness, thermal diffusion, low friction coefficient, good adhesion to the substrate, and high oxidation and wear resistance as well as fracture toughness are promising for high temperature applications such as protective coatings for cutting tools, effective diffusion barriers in microelectronics or thermal barrier coatings for gas turbines [3, 6–8]. Shortly after the discovery of the first HEAs, the first HEA and HEA nitride thin films were fabricated by PVD. HEA nitride coatings can be deposited by allowing the atoms or ions from a HEA target to react with N_2 gas during deposition. Yeh and co-workers investigated the diffusion kinetics of transition HEA thin films fabricated by MSD in different gas atmospheres as potential candidates for diffusion barriers [7, 24–29]. Dolique et al. deposited and characterized magnetron sputtered AlCoCrCuFeNi HEA thin films by tailoring the composition of mosaic targets [30, 31]. Subsequently, more and more studies on HEA and HEA-based coatings have been performed and reported because of their high potential for achieving promising properties. Depla and co-workers conducted studies on magnetron-

sputtered HEA thin films in different gas atmospheres and by engineering the composition of the constituting elements in the pressed powder targets [32–35]. Yalamanchili et al. investigated the thermal stability of (AlCrNbTiV)N synthesized by reactive CAD [36].

Refractory HEAs are promising for ultra high temperature applications due to the high melting temperatures of up to 3500 °C and high temperature strengths of the constituting elements [28, 37]. Malinovskis et al. and Johansson et al. characterized (CrNbTaTiW)C and refractory (HfNbTiVZr)N coatings, respectively, synthesized by MSD [38, 39]. Lee et al. conducted studies on thermal, high temperature electrical and oxidation properties of MoNbTaVW thin films [40].

PVD techniques including CAD and MSD are feasible for the fabrication of HEA and HEA based coatings with desired properties [41]. Other thin film fabrication techniques include thermal spraying, gas tungsten arc welding, ion plating and laser cladding. This thesis will mainly focus on HEA thin films synthesized by selected PVD techniques which will be described in detail in Chapter 3.

3 Coating synthesis

Nowadays, the majority of the industrially produced coatings are fabricated either by chemical or physical vapor deposition. Within this work, beside HiPIMS, the most common PVD techniques such as MSD and CAD were applied. Depending on the target material, MSD and HiPIMS exhibit smoother coatings as compared to CAD, while the latter achieves higher deposition rates. As all three deposition methods were used within this work to synthesize HEA thin films, some aspects and characteristics of the methods are described in this chapter.

3.1 Electrical discharges

PVD techniques utilize electrical discharges passing as an electrical current through a normally insulating medium creating a plasma. Plasma can be envisioned as a kind of fluid conductor between the electrodes, which by definition is quasi-neutral (i.e., the amount of positive and negative charge is equal in a given volume of consideration) [42]. Low pressure electric discharges are created by electric current flows in an insulating gas between two electrodes, due to the presence of charge carriers, e.g. thermal electrons or gas atoms ionized by cosmic radiation, creating a current of nA or less. The resulting electrical field between the electrodes is not high enough to accelerate free electrons up to kinetic energies sufficient to ionize gas atoms by collision. The latter is the first regime in the voltage–current characteristic shown in Figure 3.1. The Townsend discharge is a non-luminous, self-sustaining discharge, characterized by low electron densities and low currents up to 10^{-6} A [43, 44]. A further increase in current results in a drop of voltage and more efficient ionization processes forming the glow discharge regime. In this region, the current steadily increases until the whole cathode surface is affected by ion bombardment and shows a uniform current density. Sputter deposition using magnetically enhanced glow discharges normally operate in the abnormal glow region [45]. Arc discharges are characterized by high discharge currents (starting from a few A) and low voltage (typically 20 to 30 V). An arc can also be directly ignited by other means, e.g. by the separation of connected (short-circuited) electrodes. It does not require a background gas and can be operated in vacuum, but also at atmospheric pressure and beyond [44].

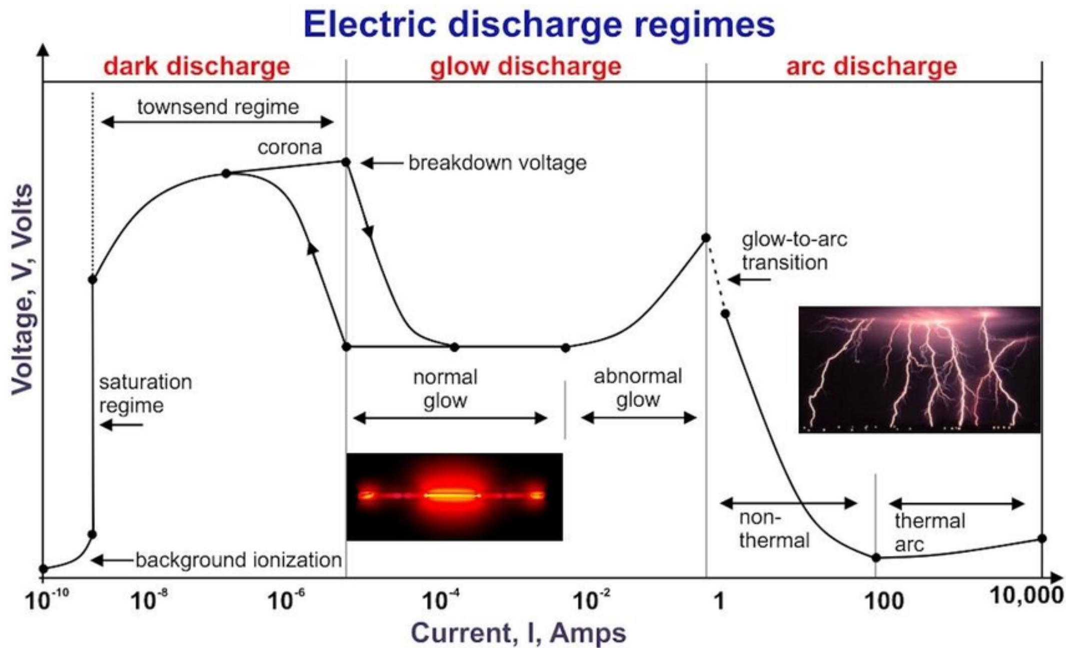

Figure 3.1: An overview of the voltage–current characteristic of different gas discharges shown by Druyvesteyn and Penning [46]. The corresponding discharge types and the breakdown voltage are indicated and adapted from [43].

3.2 Sputter deposition

3.2.1 Physical basics

Sputtering is described as non-thermal vaporization of atoms caused by the bombardment of energetic particles as schematically shown in Figure 3.2 [47]. Sputter deposition refers to the transport of the vapor from the target towards a substrate and finally the condensation of the vapor on the substrate. The bombarding particles are ions typically originating from a gas discharge hitting the target surface region. Depending on the energy of the incident ions, their mass, the mass of the target atoms as well as the surface binding energy of the target atoms, several processes may occur. Ions bombarding the surface are neutralized, reflected, implanted into the near surface region or create a collision cascade, where some of the momentum is transferred to a surface atom leading to the emission of a target atom. These "sputtered" atoms may condense on a substrate placed in the stream of ejected atoms to form a thin film. Sputtered atoms are influenced by several parameters including ion energy, ion to atom mass ratio,background (working) gas pressure, incoming angle and surface energy. The most common form of sputtering is the plasma-assisted sputtering, where positive ions, like Ar^+, are accelerated towards the negatively biased target with respect to the plasma, typically between 300 to 700 V [44, 48]. The sputtered particles typically have energies

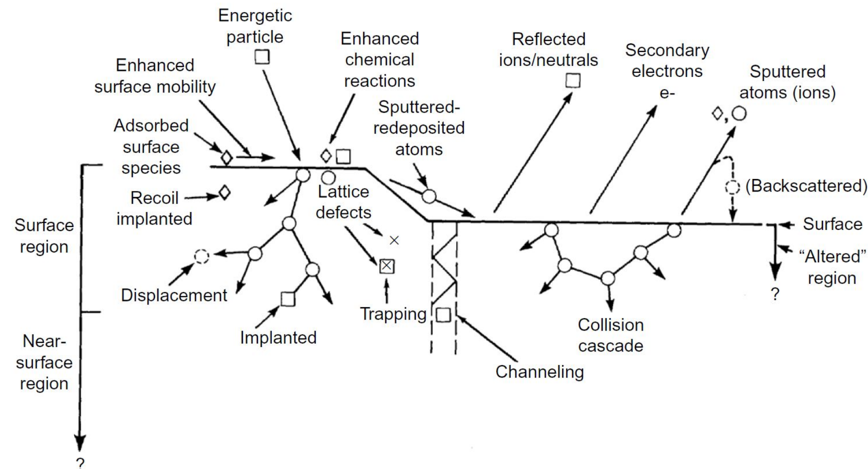

Figure 3.2: Interaction of energetic particles bombarding a target surface [50].

ranging from 5 to 40 eV [49]. The ionization of the Ar atoms takes place by inelastic collisions with electrons. Secondary electrons, generated by the Ar^+ bombardment of the target surface, are able to further increase the ionization of the Ar atoms. The plasma created due to the excitation of the gas atoms by the electrons is luminous in the visible and, hence, it is called a glow discharge. The term sputter yield is used to describe the efficiency of the sputtering process, which correlates to the number of ejected atoms per incident ion [47, 49, 50].

3.2.2 Magnetron sputter deposition

Magnetron sputter deposition represents a typical plasma-assisted thin film deposition technique within the group of PVD methods. Despite high film quality, the strengths of MSD are its flexibility and the ability of depositing coatings under strongly non-equilibrium conditions. This allows the deposition of even immiscible elements and almost any coating material can be synthesized with properties that are not frequently achievable in bulk materials. Magnetron sputtering is based on dc diode sputtering using the principle of sputtering, as described in Section 3.2.1. Diode sputtering is nowadays very rarely employed due to several limitations like the low ion current density and, thus, low plasma density and deposition rate plus the large substrate heating effects [49–52]. In order to compensate the above mentioned shortcomings, magnetrons were developed to achieve sufficiently high plasma densities in front of the target and, hence, high erosion. The term "magnetron" derives from the installed magnets behind the targets which generate a magnetic field in the vicinity of the target, increasing the ionization rate in this region by trapping secondary electrons emitted

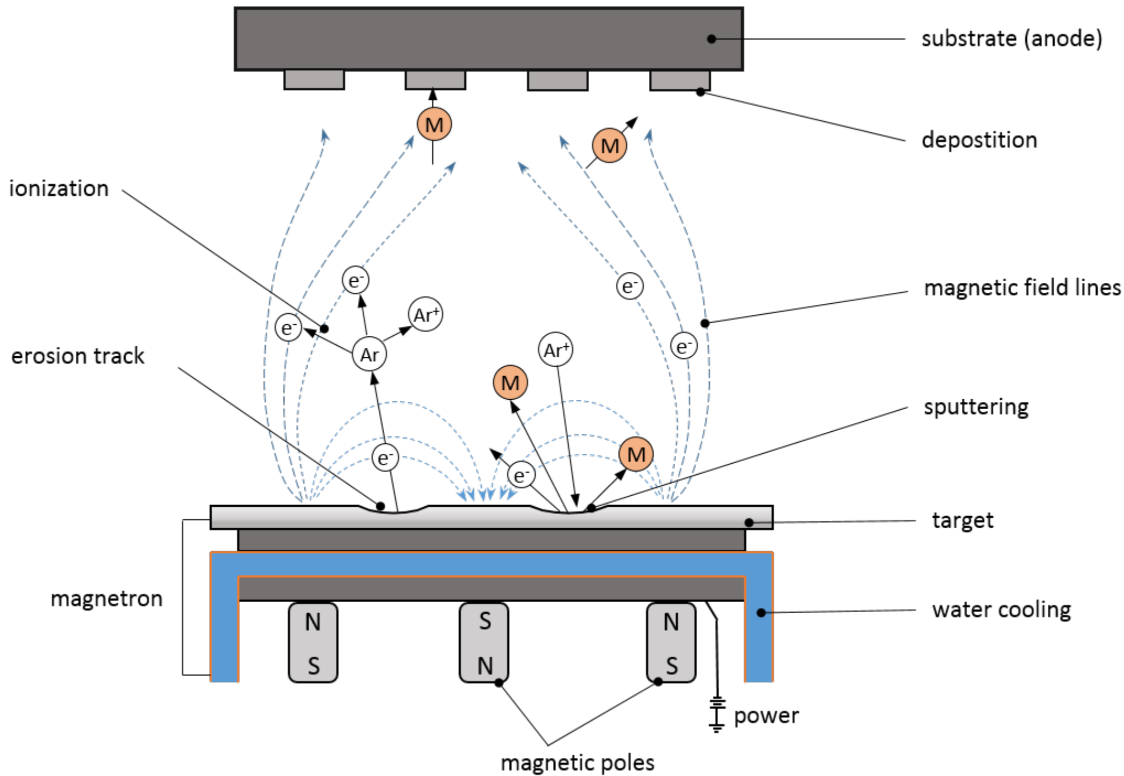

Figure 3.3: Schematic illustration of an unbalanced magnetron sputter deposition system, modified after [53].

from the target surface due to the ion bombardment. For an optimized electron confinement, the magnetic field B needs to be parallel to the substrate surface. Hence, there are two magnetic rings installed in a typical planar circular target, one outer and one inner pole ring of opposite polarization to generate a magnetic field configuration as depicted in Figure 3.3. This set-up significantly enhances the electron flux, increases the ionization efficiency of Ar atoms and leads to a high density plasma. The region of the most intense plasma is named "racetrack", where the electric field E and the magnetic field B are perpendicular to each other and thus form a maximum of the Lorentz force, providing an effective confinement for electrons [47, 49, 50, 52, 53]. MSD, with the exception of radio frequency sputtering, is a PVD process that allows the sputtering of electric conductive materials with a reasonable combination of coating surface quality and deposition rate. Therefore, it has been established for decades as a reliable process of choice in many different applications in research and industry. Thin films fabricated using the above mentioned techniques are, e.g., optical coatings used for mirrors or architectural glass, wear-, erosion-resistant or tribological coatings for cutting tools, corrosion-resistant coatings and functional thin films used in flat panel displays and microelectronics [49, 50, 54].

High power impulse magnetron sputtering

Developed by the Russian scientist Vladimir Kouznetsov, the novelity of the HiPIMS technique is the production of high density plasmas with a high degree of sputtered atom ionization [55]. HiPIMS, also known as HPPMS (high power pulse magnetron sputtering) is a PVD technique in which the power applied to the target is in pulses of low duty cycle ($<$ 10%) and frequency ($<$10 kHz) leading to very high target peak power densities of several kWcm^{-2}. The word "impulse" is used to imply very high power and very low duty cycle. The percentage of time that the processing power (negative potential on a target or substrate) is above zero is called the duty cycle. The off time is the percentage of time in which the voltage is zero or positive [50]. Generally, the HiPIMS discharge operates with a pulsed target voltage of 500-2000 V and target currents two orders of magnitude higher than the average target current in conventional sputtering techniques (1.5 - 2 A), such as MSD. This results in the generation of ultra-dense plasmas with electron densities in the order of 10^{19} m^{-3}, which are much higher than the values of 10^{14} - 10^{16} m^{-3} commonly obtained for MSD in the vicinity of the target [54, 56]. Thus, the probability for electron-impact ionization of sputter-ejected atoms is increased and ionization levels can be up to 90% [56]. However, due to overheating, the average HiPIMS power should not exceed the level of conventional MSD in which the plasma is dominated by gas ions [57]. Figure 3.4 depicts typical voltage and current waveforms measured during a HiPIMS pulse within this work at 600 V and at a peak target current of 70 A. The average power applied for HiPIMS was 500 W with a pulse length of 200 μs and a pulse repetition frequency of 100 Hz resulting in a peak power density around 930 Wcm^{-2} on a total target diameter of 7.6 cm. These features enable the deposition of dense and smooth coatings on complex-shaped substrates, and provide new and added parameters to control the deposition process, tailor the properties and optimize the performance of elemental and compound films [48, 54]. Due to the high degree of ionization of the sputtered species, particularly adhesive and dense films can be obtained when a bias voltage is applied to the substrates. However, the major drawback of this technology is the considerably lower deposition rate as compared to MSD, which is mainly due to the fact that a considerable fraction of the newly formed ions returns to the target and not contributes to the film growth [58].

3.3 Cathodic arc deposition

CAD is a PVD method that utilizes arc discharges to vaporize material from the surface of an electrode (cathode). Nowadays, CAD is a common industrial PVD process to produce

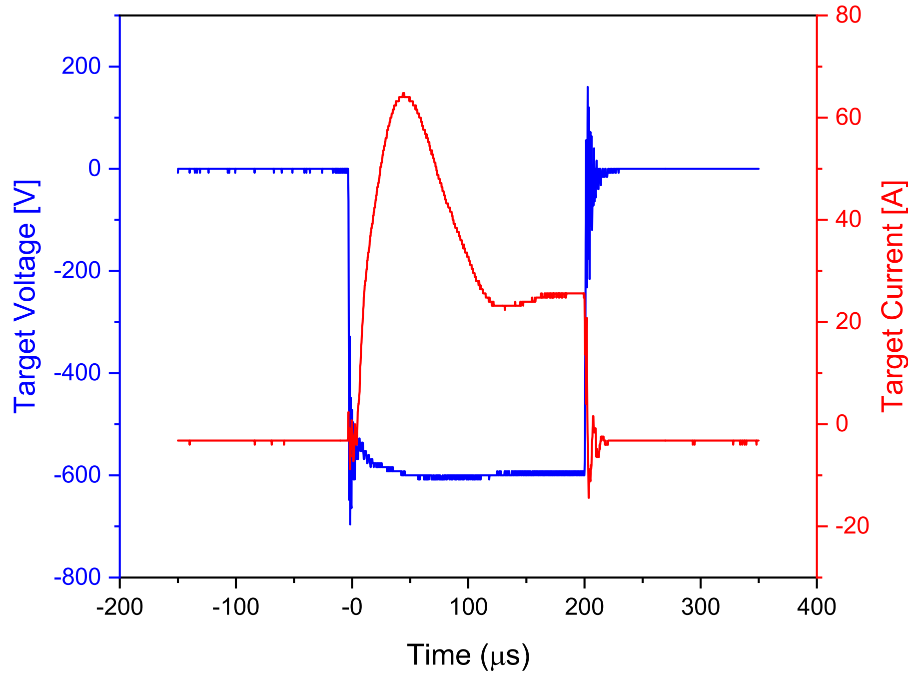

Figure 3.4: Voltage and current waveforms recorded during HiPIMS operation using a 200 μs long pulse. The data were recorded by the author of this thesis during HiPIMS deposition of a MoNbTaVW HEA thin film in Ar atmosphere.

decorative and corrosion-resistant thin films as well as hard coatings on cutting tools as more favorable deposition characteristics can be achieved as compared to, e.g., MSD and HiPIMS. Among the reasons for the interest in CAD are: the high deposition rates achievable for metal and compound films; generally good to very good adhesion of coatings; the relative ease of forming hard and decorative coatings and the relatively wide range of usable partial pressures of reactive gases to form stoichiometric films. Since CAD was used in dc mode to synthesize HEA thin films, some aspects and characteristics of the deposition method are described within this section.

3.3.1 Plasma generation: Cathode spot

Cathode processes are the source of cathodic arc plasma production. According to Anders [42], plasma formation in the case of arc discharges is closely related to the electron emission mechanism, which is thermally unstable thermo-field emission, i.e., a locally concentrated, non-linear superposition of field emission and thermionic emission. This is also known as explosive emission, and the apparent motion of the cathode or arc spot over the surface is in fact a sequence of rapid microscopic explosions.

Cathode spots are centers of electron emission and plasma production where ions of

the cathode material are produced. The ion contribution is crucial for the arc evaporation process as well as for establishing the plasma. These spots are small areas (~10^{-14} - 10^{-10} m^2) of very high current density (~10^{10} – 10^{12} A/m^2) and relative high power density (~10^{11} – 10^{14} W/m^2), where the cathode surface material is extremely rapidly transformed from solid to plasma due to the combined action of ion bombardment and Joule (Ohmic) heating [59]. The plasma formed at small, mobile cathode spots consists of cathode material while a process gas does not need to be present. However, Ar gas has been found to promote discharge stability, and a reactive gas is needed when the goal is to deposit compound films. In the absence of any gas one speaks of vacuum arcs [59].

Depending on the surface conditions, metallic-clean versus covered with a non-metallic layer or contamination, one can find two different types of arc spots and erosion traces [59]. Cathodes with a non-metallic overlayer (spot type 1) generate spots that move fast (1000 m/s), with small, shallow, disconnected erosion craters. They also produce small macroparticles. In contrast, arc spots on a clean metal surface (spot type 2) are relatively bright, move relatively slow (10-100 m/s), leave large erosion craters, and produce large macroparticles. As the action of the arc removes cathode material, thereby cleaning the cathode, spot types can change during the discharge. An arc could start on a non-treated, contaminated surface with spot type 1, and continues to operate on a cleaned cathode with spot type 2. For many practical applications, where compound films are needed, one adds a reactive gas into the deposition chamber to intentionally "poison" the cathode, i.e. to form a compound layer and thereby letting the arc burn with type 1 cathode spots. While the deposition rate is reduced in the "poisoned" mode, it is still high enough to be economically relevant. Furthermore, by "poisoning" the cathodes, large macroparticles can be avoided.

3.3.2 Macroparticles

During conventional CAD, thin film synthesis is typically accompanied by the incorporation of numerous macroparticles, also known as droplets. Macroparticles are named this way to emphasize their very massive nature compared to electrons and ions and they are typically associated with the reduction of the coating quality. As schematically shown in Figure 3.5, macroparticles are liquid or solid debris particles that are produced at cathode spots along with the plasma. Macroparticles form when the layer of liquid cathode material (in black) yields to the plasma pressure and they are preferentially ejected under 5–30° parallel to the cathode surface. Just-ejected macroparticles may rapidly cool down and freeze at the crater rim, forming microprotrusions that can serve as field-enhancing objects for the ignition of the next emission site. Macroparticles sticking to the substrate usually form a round or donut-

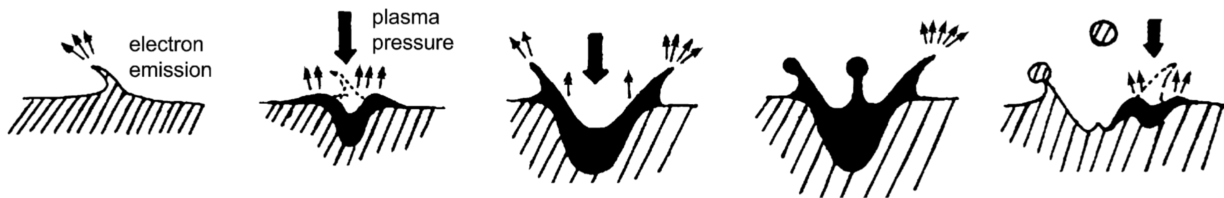

Figure 3.5: An illustration of macroparticle generation as a result of plasma pressure on the liquid cathode material [42]

.

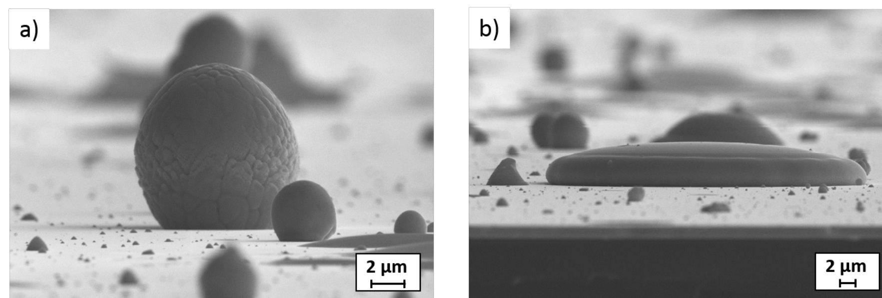

Figure 3.6: Macroparticles formed on Si substrates during CAD of MoNbTaVW HEA thin films are observed to be a) spherical and b) donut-shaped [42] (Photo courtesy of Giovanni Bolelli, University of Modena and Reggio Emilia, Italy)

like shape depending on the impact energy as shown in Figure 3.6 [42]. As a rule, materials with low melting point produce more and larger macroparticles and it is therefore more likely that they form thin film surfaces with matt appearance in comparison to elements with higher cohesive energy or melting temperature. Even though coatings fabricated by CAD contain droplets, which weaken the film homogeneity. As the incorporation of droplets leads to the formation of growth defects that extent through the remainder of the coating, they still show good film properties [60]. Depending on the cathode material, macroparticles may not effectively stick but rather "bounce" off the substrate's surface. Typical examples for such an effect are carbon and refractory metals. In fact, macroparticles may be reflected several times before they ultimately rest on the substrate surface. These attached macroparticles may be coated by the growing thin film causing a defect by forming a severely underdense microstructure near the lower part of the droplet [60], as shown in Figure 3.7. Similarly, detached macroparticles also cause a defect in the growing film by leaving holes in the thin film [47]. The resulting defects corrupt the mechanical, tribological, optical and other thin film properties. Although the amount of macroparticles can be reduced by using arc filters, the addition of filters is technically difficult and it is usually associated with a reduction in deposition rate and increase in film stress [42].

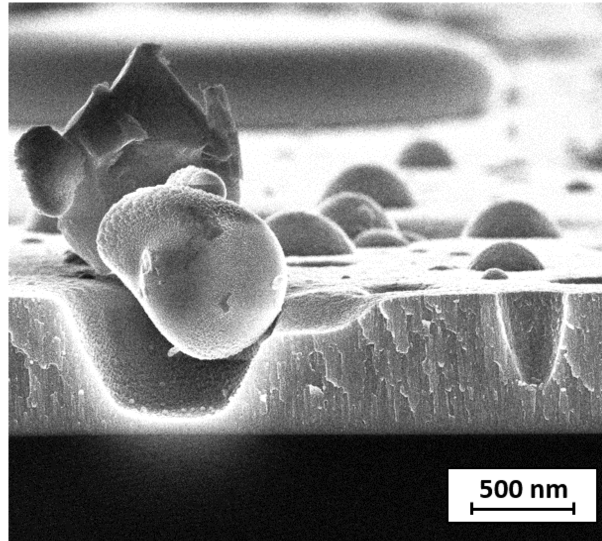

Figure 3.7: Incorporation of a large macroparticle in an AlCuCrTaTi HEA thin film. (Photo courtesy of Giovanni Bolelli, University of Modena and Reggio Emilia, Italy)

3.3.3 Arc source design and magnetic fields

Arc discharges can be continuous or pulsed and are characterized by a high electrical current, low voltage passing through a gas or vapor of the electrode material. Most of the ejected material is thermally evaporated atoms but some is ejected as molten droplets or solid particles from the cathode. The applied high current density heats the electrodes. A high percentage of the evaporated atoms are ionized in the arc evaporation process because of the high electron density. Continuous arc plasmas contain a great amount of neutrals from evaporating macroparticles and cooling spot craters. Therefore, dc arcs have generally lower mean ion charge states and ion energies, which may have consequences for the film properties.

Figure 3.8 depicts the basic arrangement of a typical arc source. In such devices, the source serves as cathode, while the chamber wall normally acts as anode. A mechanical trigger is attached to the cathode to start the deposition process by igniting the arc discharge. The arc spot moves along the cathode surface and consumes cathode material by transforming it into charged or neutral species in vapor form or particles. Normally, the cathode is enclosed by a ceramic insulator. This contains the formation of arc spots to the cathode surface and avoids contamination by evaporating other machine parts or even complete destruction of the device. Should the arc spot move into the narrow gap between cathode and electric insulator, the impedance goes up and the operation of another spot on the front face is re-established. The anode, on the other hand, solely acts as an electron and particle collector [42, 50].

There are a few important requirements for an arc source design, which are dissipation of the heat generated by the arc spot, confinement of the arc to the appropriate cathode surface and the anode must carry the arc current.

According to Anders [42], typical arc currents are between 40 and 150 A. By increasing the arc current higher than 150 A, proportionally higher plasma production and deposition rate can be achieved. However, the biggest issues appearing with high current is the cooling problem of the plasma source and the substrate, increased costs for the power supply, and higher macroparticle contents of the coatings.

According to literature [42, 50], ~1/3 of the total arc supply power is converted into heat and, therefore, it is common to use water cooling systems mounted on the back of the cathode in industrial deposition devices.

In the absence of a magnetic field, the cathode spot moves randomly over the cathode surface. Most sources, however, apply some means of spot steering, either by magnetic or by electric means to better control the spot motion. In the presence of a magnetic field, the spot motion can be described by the retrograde motion rule $-(\mathbf{j} \times \mathbf{B})$ with the vector of current density $\mathbf{j}$ normal to the surface and the vector of magnetic induction $\mathbf{B}$, given by the presence of permanent magnets or magnetic field coils. Other factors that influence the spot motion are the background gas pressure, the cathode temperature and, to a limited extent, the cathode material [42]. According to the steered arc source classification by Karpov [61], two basic magnetic field configurations are distinguished: "through-field" and "arched field" configurations, as shown in Figure 3.9. Similar to ordinary magnetrons for sputter deposition, the fields are generated by coils or permanent magnets placed behind the cathode and optimizations are adapted with regard to the cathode material. However, one should consider the material utilization factor and not erode through the cathodes, as the arc spots tend to erode the same racetrack area that is preferably evaporated [42, 61].

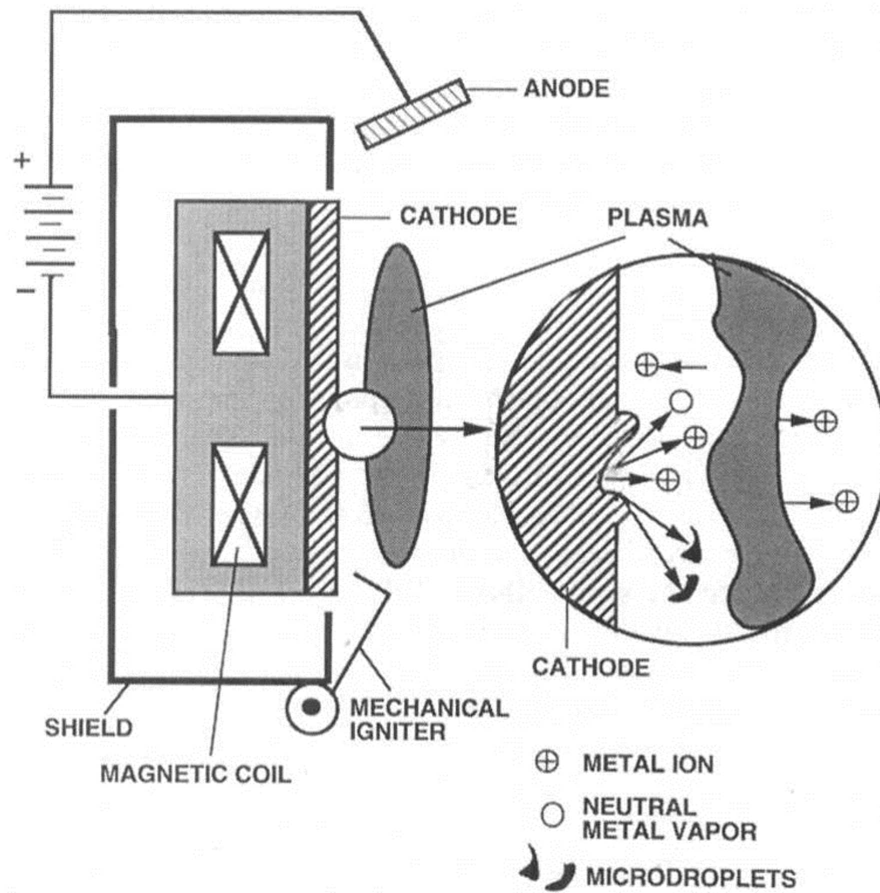

Figure 3.8: Schematic outline of a cathodic arc source and the plasma that is produced by the cathode spot [49].

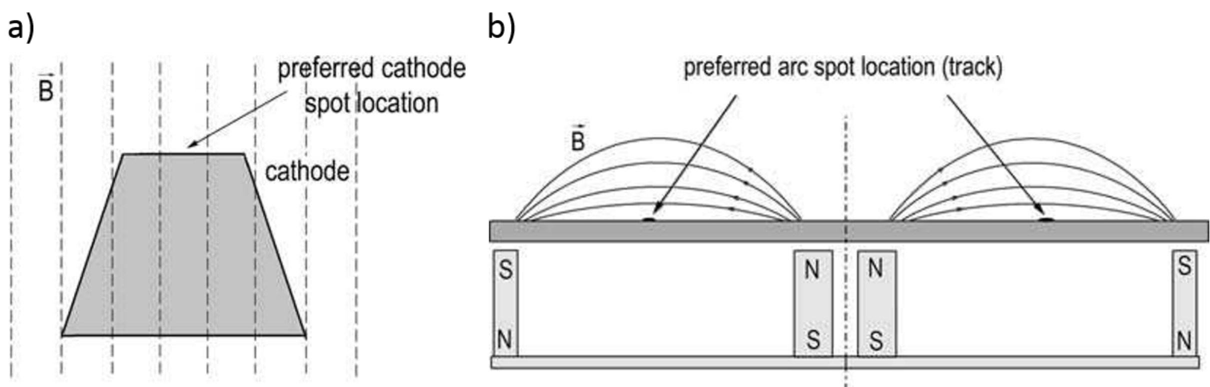

Figure 3.9: Illustration of possible internal magnetic field configurations used for steering of the cathode spot: a) through-field and b) arched field configuration [42].

4 Methods

The methods presented in the following section have partly been published by the author in [62–64].

Thin film deposition by MSD, HiPIMS and CAD was performed in the same lab-scale deposition system. Equiatomic $Mo_{0.20}Nb_{0.20}Ta_{0.20}V_{0.20}W_{0.20}$ targets for MSD and HiPIMS (∅ 76 mm × 6 mm) as well as cathodes for CAD (∅ 65 mm × 12 mm) were powder metallurgically produced by Plansee Composite Materials GmbH, Germany. 325 μm thick B doped (100) Si, 50 μm thick PI (UBE UPILEX-S 50 S) and Al_2O_3 (0001) single-crystal substrates were fixed on a grounded substrate holder at a distance of up to 25 cm to the cathode surface. Prior to deposition, the substrates were ultrasonically cleaned in an ethanol bath for 7 min and afterwards air dried. No external heating or plasma etching of the substrates prior to deposition was applied.

Before deposition by CAD, MSD and HiPIMS, the chamber was evacuated to a base pressure of about 8×10^{-4} Pa. In the case of CAD, a constant Ar flow was introduced through a mass flow controller (Brooks Instrument) into the vacuum chamber to ensure a stable plasma during the deposition process. N_2 was added to synthesize MoNbTaVW nitride thin films. The total gas flow rate was kept constant at 100 standard cubic centimeters per minute (sccm) resulting in a total gas pressure of about 5 Pa. The N_2 flow ratio, R_{N_2} $=N_2/(Ar+N_2)$, was varied from 0 to 50%. For CAD, an applied current of 120 A during deposition resulted in a voltage of 26 V. In the case of MSD and HiPIMS, the same average power of 500 W was applied. For MSD, the measured voltage was 330 V resulting in a current of 1.2 A. For HiPIMS, an applied voltage of 600 V resulted in an average current of 0.7 A. The pulse length and pulse repetition frequency in the case of HiPIMS were 200 μs and 100 Hz, respectively.

The film morphology and the film thickness were analyzed from images taken with a scanning electron microscope (SEM) Zeiss Evo-50 as well as with a field emission gun scanning electron microscope (FEG-SEM) Quanta-200 and Nova NanoSEM 450 (FEI - ThermoFisher Scientific). The chemical composition of the films was obtained by energy dispersive X-ray spectroscopy (EDX) and by wavelength dispersive X-ray spectroscopy (WDX) using an Oxford Instrument INCA detector attached to the Tescan Clara SEM.

The microstructure of the as-deposited films was measured by XRD in Bragg-Bretano

geometry using a Bruker-AXS D8 Advance diffractometer equipped with Cu-K_α radiation and parallel beam optics. The samples were scanned in the range from 20 to 80° with a resolution of 0.02° per step at a step time of 1 s/step.

The biaxial film stress was determined by the wafer-curvature method using a custom-built device with two parallel laser beams [65]. The modified Stoney's equation was applied to calculate the residual stresses of the films [66, 67]. Hardness and Young's modulus of the films were measured by means of nanoindentation using a UMIS II nanoindenter by Fischer-Cripps Laboratories with a Berkovich diamond tip. Overall 15-25 load-displacement curves per sample were measured and evaluated according to the Oliver and Pharr method [68].

Changes in the electrical resistivity of the as-deposited thin films were measured with a four point probe (Jandel resistivity test unit). Details about the electromechanical behaviour of the films were obtained via in-situ uniaxial tensile straining tests using an MTS Tytron 250, which was equipped with a four point probe to record the electrical resistance during straining. Samples with a size of 35 mm × 7 mm of the as-deposited films on PI were strained with a displacement rate of 5 μm/s up to a maximum of 12% engineering strain. Further information about the crack formation was revealed from images taken during in-situ straining using an Olympus LEXT OLS 4100 Confocal Laser Scanning Microscope and Anton Paar TS 600 mobile straining device. The samples with the size of 40 mm × 8 mm were tested with the same parameters as in the previous tests.

5 Results and discussion

The results presented in the following sections have partly been published by the author in [62–64].

5.1 Angular-dependent deposition

This section analyses the same HEA thin film material, which was deposited angularly resolved by three different PVD methods, namely MSD, HiPIMS and CAD [63]. This set of frequently used PVD methods allows for comparing two sputtering techniques with low (MSD) and high (HiPIMS) degree of ionization, whereas HiPIMS and CAD both enable high energetic film growth conditions, but vary significantly in the typically achieved deposition rate. For all three different PVD methods, the respective source was positioned in the center of a cylindrical vacuum chamber (⌀ 50 cm). This geometric set-up allowed to use the entire chamber wall as substrate holder with a constant source-substrate distance of 25 cm relative to the center of the source. The deposition time was set to 120 and 180 min for MSD and HiPIMS, respectively, while applying the same average power of 500 W. The pulse length and pulse repetition frequency in case of HiPIMS were 200 μs and 100 Hz, respectively. Prior to CAD, the deposition chamber was evacuated to a base pressure of 1.8×10^{-2} Pa due to modification of the arc source for these experiments. The Ar pressure and the arc current were kept constant at 4.85 Pa and 120 A, respectively, during the deposition that lasted for 20 min. The synthesized MoNbTaVW HEA thin films were analyzed as to their chemical composition, morphology, crystallographic structure, residual stress, hardness and elastic modulus in order to elucidate the correlation between synthesis, structure and properties of HEA thin films.

5.1.1 Deposition rate

Depending on the PVD method and deposition angle, MoNbTaVW thin films with thicknesses ranging from 264 to 3200 nm were synthesized. The deposition rate of the three PVD methods as a function of angle is illustrated in Figure 5.1. For the purpose of better visualization, the actual deposition rate of MSD and HiPIMS is multiplied by a factor of 10.

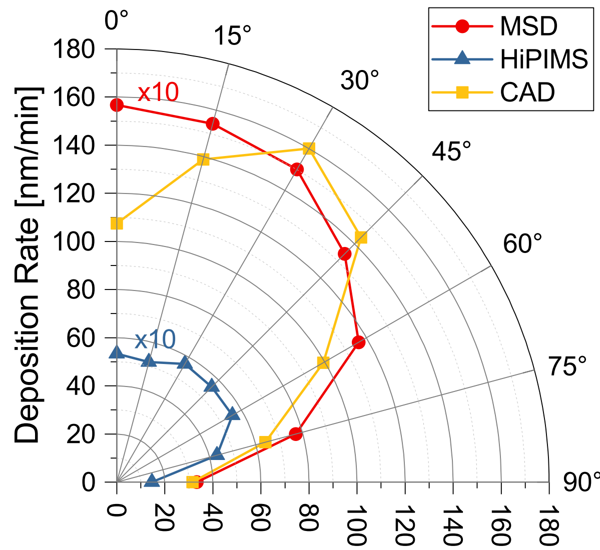

Figure 5.1: Deposition rates for MoNbTaVW thin films at different deposition angles synthesized by MSD, HiPIMS and CAD.

Even though the deposition rate of HiPIMS is only about 1/3 of the one of MSD, their angular dependence is similar. The maximum deposition rate is encountered at 0° with about 16 and 5.5 nm/min for MSD and HiPIMS, respectively. In the case of MSD, this value remains constant up to 30°, but starts to decrease at higher angles reaching its minimum of 3.3 nm/min at 90°. The deposition rate in HiPIMS remains constant up to 60° before it starts to decrease to its minimum of 1.5 nm/min at 90°.

In contrast to both sputtering techniques, the deposition rate of CAD first increases with increasing deposition angle. The maximum was encountered at 30° with 160 nm/min. At even higher angles the deposition rate decreases to its minimum value of about 32 nm/min at 90°.

5.1.2 Chemical composition

Figure 5.2 displays the chemical composition of the MoNbTaVW HEA thin films. The elements can be grouped according to their atomic mass, i.e. heavy (Ta,W), medium (Nb,Mo) and light (V).

The heavy elements in the sputter-deposited films generally show an increase in their ratio with increasing deposition angle up to 75°.

This trend is more pronounced in the films deposited by HiPIMS than the ones deposited by MSD. In contrast, the metal ratio of Ta and W in the films deposited by CAD decreases with increasing deposition angle, most prominently when changing from 0 to 15°. However,

a strong reduction in the content of the heavy elements was observed at 90° regardless of the applied deposition technique.

The metal ratio of the elements with medium mass, i.e. Mo and Nb, remains largely unaffected by changes of the deposition angle in all three techniques showing a value close to 20 at.%, i.e. reflecting the target/cathode composition used for the synthesis of the films. Minor exceptions are the slightly elevated Mo contents at low angles for MSD and at 90° for HiPIMS.

Opposite to the heavy elements, the fraction of V, the lightest element, in the sputter-deposited films decreases with changing the deposition angle from 0 to 75°. Again, this trend is more pronounced for the films deposited by HiPIMS than the ones deposited by MSD. The V content in the films deposited by CAD first shows a strong increase when changing the angle from 0 to 15° and then a gradual increase up to 75°. At 90° a pronounced increase in V content was observed for all films regardless of the applied deposition technique.

5.1.3 Morphology

FEG-SEM cross section and surface images for the MoNbTaVW thin films obtained by all three PVD methods at 0°, 45° and 90° are depicted in Figure 5.3 revealing a columnar grain structure for all PVD methods. In the case of MSD, the images of the surface feature a strongly faceted surface at 0° (Figure 5.3a). However, with increasing deposition angle, a grain refinement is noticed as exemplified for 45° (see Figure 5.3b) where more grain boundaries are visible. At 90° mainly fine facets are observed thus indicating a greater amount of grain boundaries and a less dense film (Figure 5.3c). Conversely, HEA thin films deposited by HiPIMS generally show a fine grained, feather-like morphology and apparent smoother surface than the MSD films (see Figure 5.3d-f). With increase in deposition angle, similar to MSD, the columns appear to reduce in width. As shown in Figures 5.3g-i, apart from growth defects caused by the incorporation of macroparticles, the films deposited by CAD show a similar morphology as the films deposited by HiPIMS, but the width of the columns seems to be reduced even further.

5.1.4 Structure

XRD diffractograms displayed in Figure 5.4 reveal a bcc crystal structure for all three deposition methods regardless of the deposition angle. In the case of MSD, the XRD diffractograms of the films reveal a dominant (110) peak next to a less intensive (211) peak at 0° deposition angle. With increasing deposition angle, the intensity of the (211) peak slightly decreases

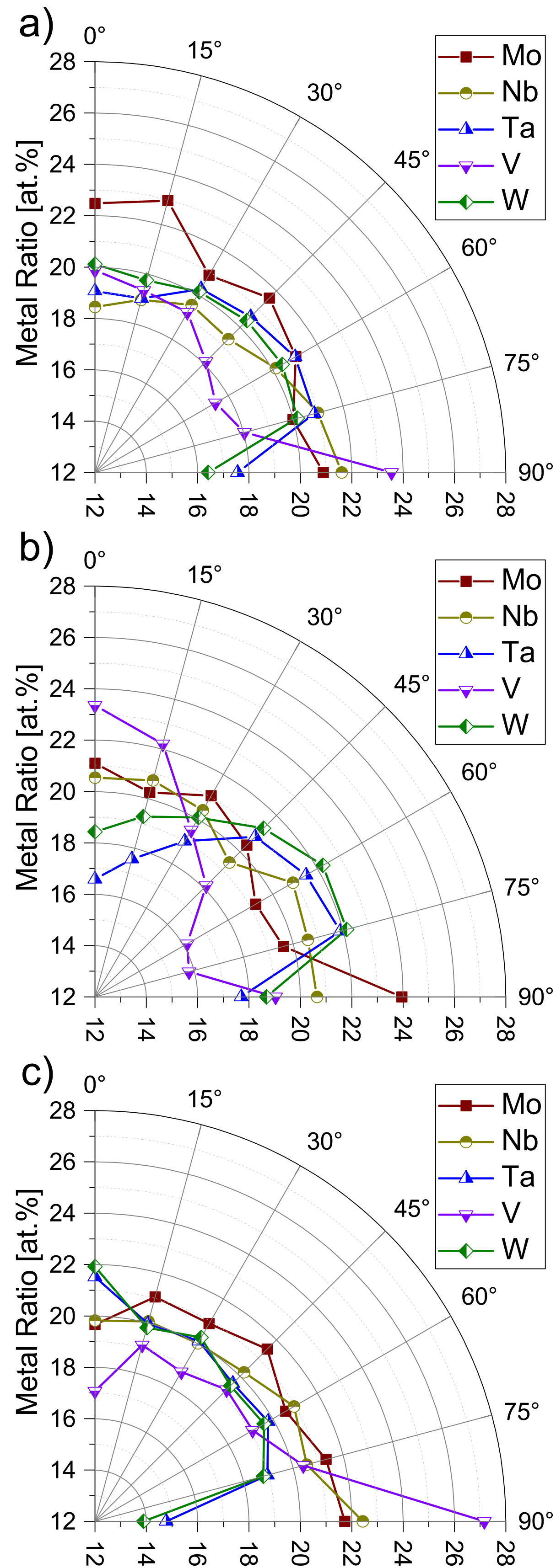

Figure 5.2: Chemical composition obtained by EDX for MoNbTaVW thin films synthesized at different deposition angles by a) MSD, b) HiPIMS and c) CAD.

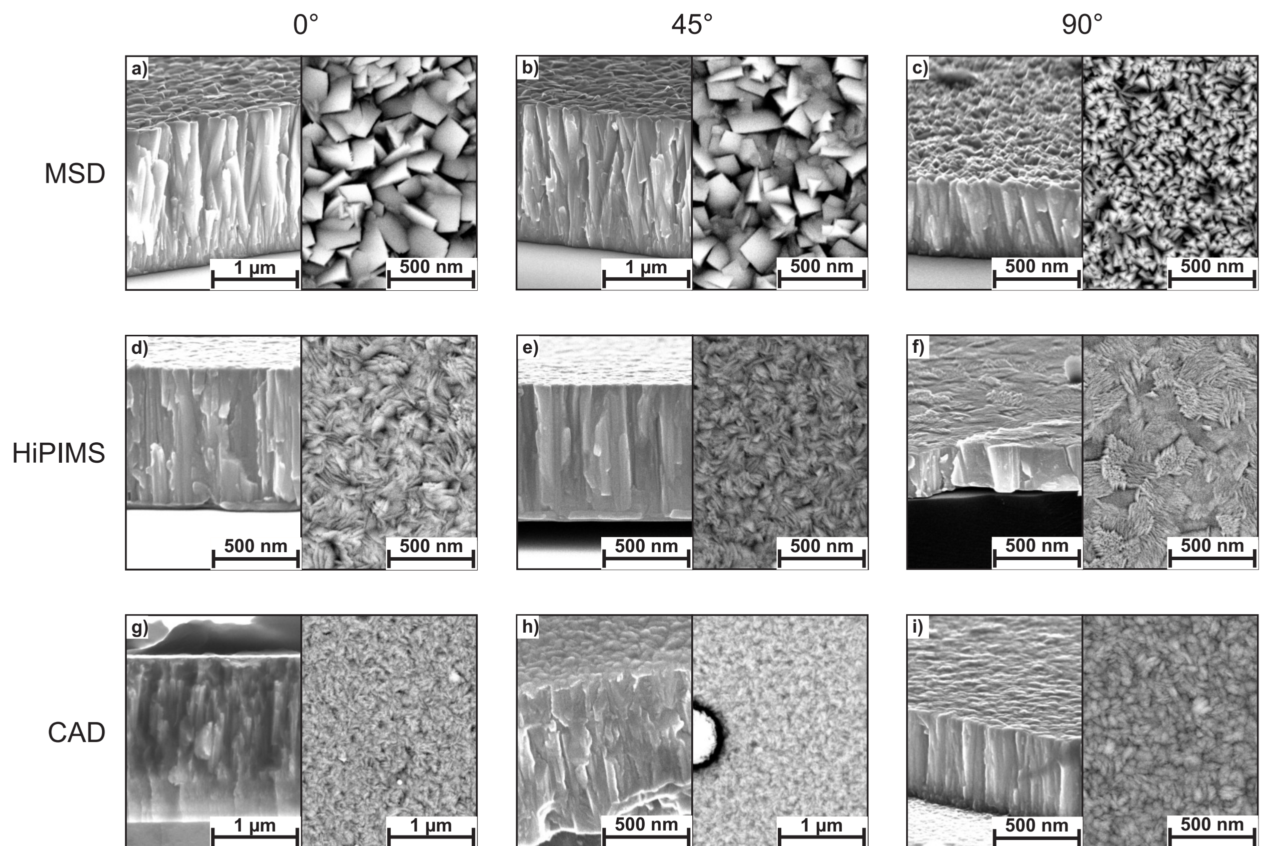

Figure 5.3: FEG-SEM cross section (left) and surface images (right) of MoNbTaVW thin films deposited by MSD (a-c), HiPIMS (d-f) and CAD (g-i) at 0°, 45° and 90° deposition angle.

up to 45°, before it starts to rise again. At 90° deposition angle, a peak originating from the Si substrate becomes visible due to the reduced film thickness. The XRD diffractograms recorded from the MoNbTaVW films synthesized by HiPIMS and CAD show a similar evolution with increasing deposition angle. In these cases, the intensity of the (211) peaks is lower than in the case of MSD. The intensity of the (200) peaks remains low regardless of deposition angle and PVD method. Due to the generally lower film thickness in the case of HiPIMS, peaks originating from the Si substrate are visible at several deposition angles.

The angularly resolved lattice parameter as derived from the (110) peak positions is depicted in Figure 5.5a. A gradual increase in the lattice parameter is observed with increasing deposition angles up to 75° for all 3 PVD methods. This increase is most pronounced in the films synthesized by HiPIMS. At the maximum deposition angle of 90°, a reduced lattice parameter for all films was noticed. In general, all obtained lattice parameters are within the range of the lattice parameters of the thermodynamically stable bcc phases of the constituting elements indicating the formation of solid solution phases. Figure 5.5b shows the theoretical lattice parameter based on the chemical composition, i.e. as a function of the metal ratio in the films. While for MSD and HiPIMS the theoretical lattice parameter slightly increases with increasing deposition angle from 0 to 75°, it remains basically constant in the case of CAD. A slight reduction is noticed in all cases at a deposition angle of 90°. Further, the theoretical lattice parameter for the films deposited by HiPIMS and CAD is significantly lower than the parameter derived from the XRD measurements. Only in the case of the films deposited by MSD, both values are in good agreement.

5.1.5 Mechanical properties

The residual stresses of the MoNbTaVW HEA thin films on Si deposited at different deposition angles are illustrated in Figure 5.6. All films deposited by MSD show tensile stresses regardless of the deposition angle. The stress values decrease from about 600 to about 250 MPa with increase in deposition angle from 0 to 75°. Compressive stresses were observed in the films deposited by HiPIMS and CAD with a general trend of increasing compressive stress for increasing deposition angle up to about 60°. The maximum values for HiPIMS and CAD were -1570 and -870 MPa, respectively. In the case of HiPIMS, the formation of spontaneous buckles (in some cases with cracks at the apex) due to high local stresses was observed for deposition angles ranging from 30 to 75° causing a release of the compressive stresses as exemplified in Figure 5.6b. When the deposition angle approached 90°, a reduction in compressive stress was noticed resulting in stress-free films or films in tensile stress states for all applied deposition techniques.

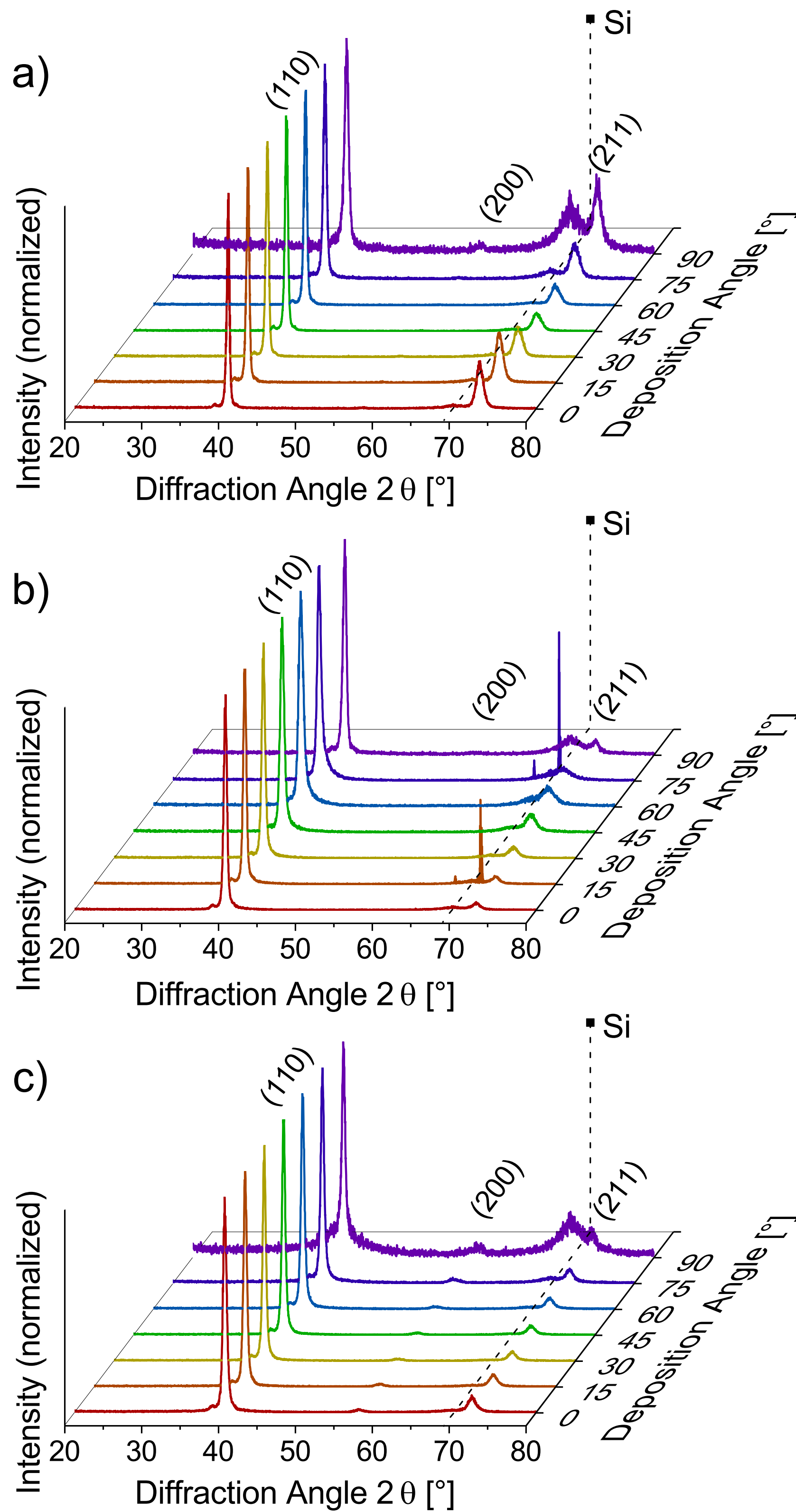

Figure 5.4: XRD diffractograms obtained in Bragg-Bretano configuration of MoNbTaVW thin films deposited by a) MSD, b) HiPIMS and c) CAD at deposition angles ranging from 0° to 90°.

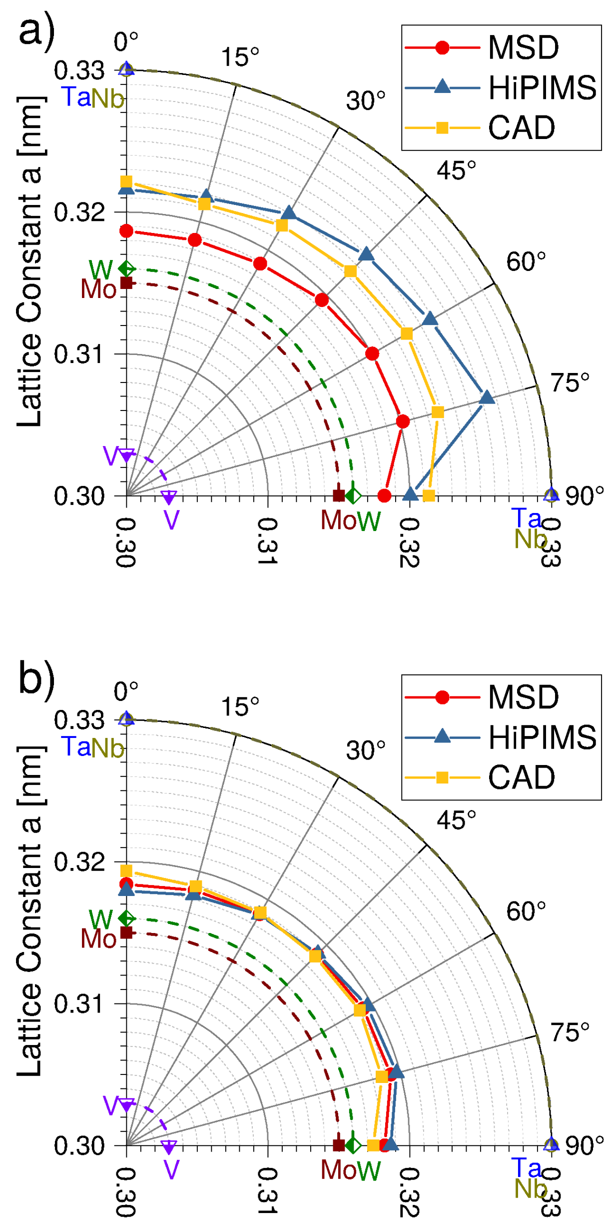

Figure 5.5: Calculated lattice constant a of MoNbTaVW thin films synthesized by MSD, HiPIMS and CAD, at deposition angles ranging from 0° to 90°: a) from XRD diffractograms and b) relative to the metal ratio of the film. Reference lattice parameters are according to [69].

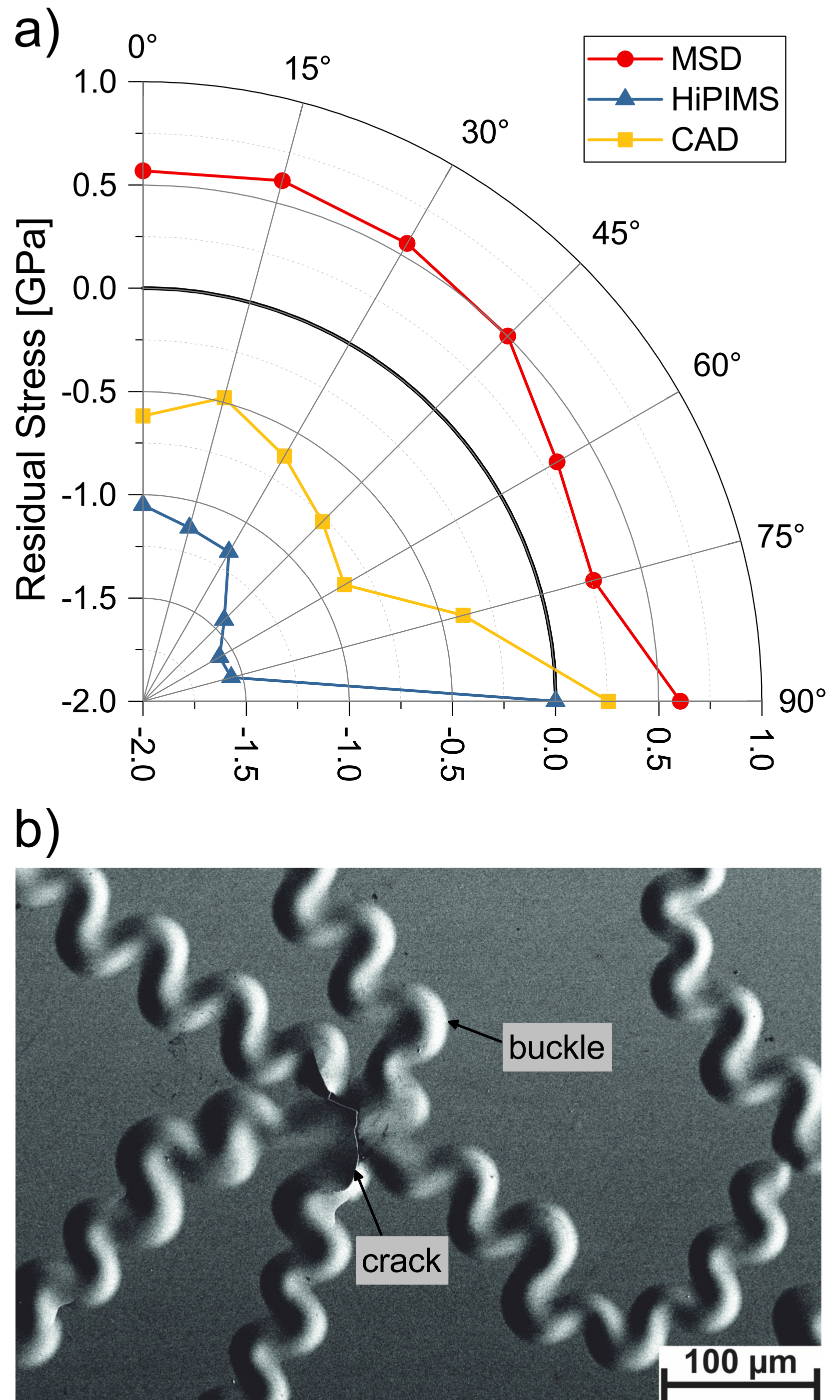

Figure 5.6: a) Film stress of MoNbTaVW thin films at different deposition angles obtained by CAD, MSD and HiPIMS. b) Spontaneous buckles formed at the surface of the MoNbTaVW thin film obtained by HiPIMS at 75°.

Values for hardness and Young's modulus for the MoNbTaVW thin films as obtained by nanoindentation are depicted in Figure 5.7 at deposition angles ranging from 0 to 90°. Overall, the films deposited by MSD show the lowest hardness, whereas the maximum values were observed for the films deposited by CAD. In terms of angular dependence, the hardness values generally increase gradually with increasing deposition angle. The reduction when exceeding 60 and 75° for the films deposited by CAD and HiPIMS, respectively, results in similar hardness values of all films at 90° ranging from 13 to 15 GPa regardless of the deposition technique. Due to the low film thickness of the samples deposited at 90°, an influence of the substrate to the hardness values cannot be completely excluded. Hardness and elastic modulus of (100) silicon at room temperature were reported to be about 13 GPa [70] and 180 GPa [71], respectively. The obtained values for the Young's modulus differ less than the ones for hardness when changing the deposition technique and are generally in the range from 200 to 250 GPa. With increasing deposition angle, the Young's modulus of the films remains constant up to 60°. At higher angles a reduction in Young's modulus was observed, which is most pronounced for the films deposited by CAD.

5.1.6 Discussion

By comparing the deposition rates of all 3 PVD methods it is observed that the deposition rate of CAD is by a factor of 10 larger than that of the two sputtering techniques, i.e. MSD and HiPIMS, which is in agreement with literature [59]. Further, the deposition rate of HiPIMS is known to be low when compared to conventional sputtering [57, 72]. The widely recognized reasons for the low deposition rate in the HiPIMS mode are the return of newly formed sputtered ions to the target and the energy dependence of the sputter yield [73, 74].

Studies comparing the density of thin films grown by MSD and HiPIMS using SEM images have already been conducted. Lundin et al. observed a densification through transition from a columnar structure to a globular nanocrystalline microstructure for thin films synthesized by MSD and HiPIMS, respectively [75]. Samuelsson et al. demonstrated a higher film density in films deposited by HiPIMS with less pronounced columnar miccrostruture and smooth surface, wherease MSD thin films exhibited a porous microstructure and rough surface [72]. Similarly, the FEG-SEM images of the MoNbTaVW HEA thin films in Figure 5.3 indicate a lower density of the films deposited by MSD than those deposited by HiPIMS. In the case of CAD, the recorded FEG-SEM images also indicate dense films. The high density of the films deposited by HiPIMS and CAD can be understood by the highly energetic film growth conditions present in these methods [59]. However, conclusions regarding the film density derived solely from FEG-SEM images should be handled with care, since apparently

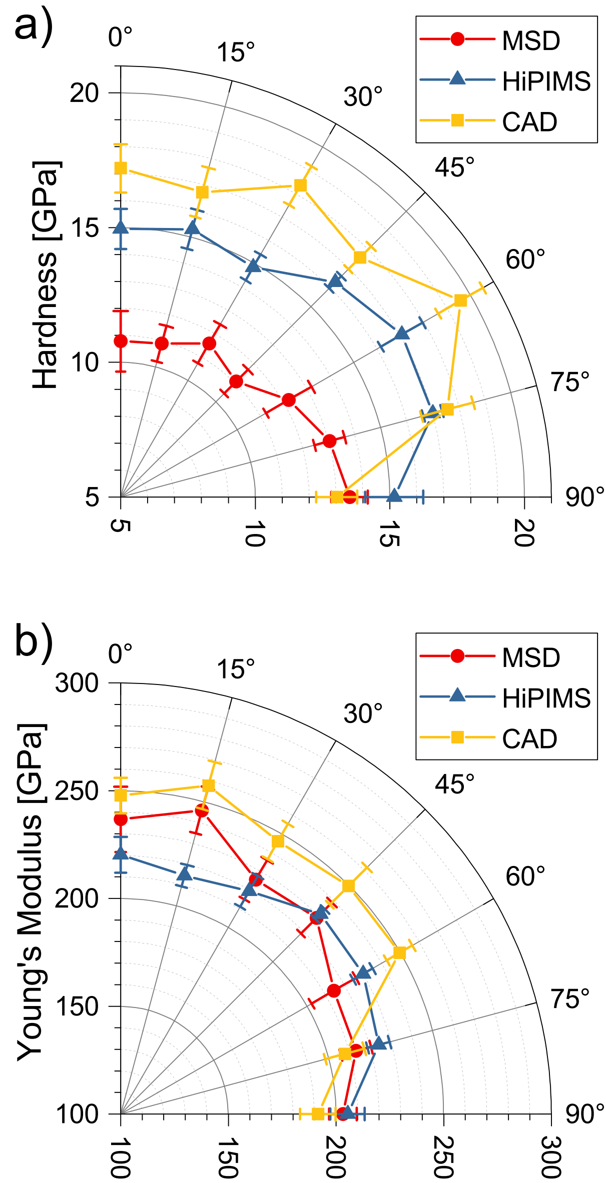

Figure 5.7: a) Hardness and b) Young's modulus values for MoNbTaVW thin films at deposition angles between 0° and 90° deposited by CAD, MSD and HiPIMS.

dense films in FEG-SEM images could contain microvoids or other underdense areas, which can only be resolved by transmission electron microscopy investigations.

The differences in the film growth conditions present in the three PVD methods also affect the crystal structure and the mechanical properties which are closely related. The larger the out-of-plane lattice constant derived from the XRD results, the higher the in-plane compressive stress. Hence, small lattice constants were noticed for the films deposited by MSD with tensile stresses and large ones for the films synthesised by HiPIMS with compressive stresses up to -1.6 GPa. The influence of the stress state on the lattice constant is more pronounced than the influence of varying chemical composition with, e.g., changing deposition angle. Similar to the residual stress in the films, also the hardness shows a variation with respect to the PVD method. However, the fact that the films deposited by CAD present a higher hardness than the films deposited by HiPIMS, even though the opposite is true for the compressive stress values, indicates that the film density influences its hardness. As higher hardness values can be expected for denser films, it appears that the MoNbTaVW films deposited by CAD are denser than the ones deposited by HiPIMS. This notion is in agreement with the cross-sectional analysis by FEG-SEM, where indications for a higher CAD film density were also noticed.

Pronounced variations with respect to the deposition angle are mainly noticed for the deposition rate and the chemical composition. The gradual decrease in deposition rate for MSD is in agreement with literature [76–80]. However, in the case of HiPIMS, the deposition rate remains constant up to 60° deposition angle. This is in contrast to other reports, where a similar decrease in deposition rate for HiPIMS with increase of deposition angle as for MSD was observed [81, 82]. A possible explanation might be due to the variation in chemical composition of the synthesized MoNbTaVW films at the different deposition angles. The elements analyzed in literature (Cu [81] and Ti [82]) have atomic masses similar to Ar and, in fact, the V metal ratio in the MoNbTaVW films shows an angular variation comparable to the reported angular deposition rates of Cu and Ti. Investigations of the angular distribution of sputtered particles from multi-element targets like alloys or compounds typically revealed an enhanced emission of the lighter element close to the target surface normal [76–78, 83]. This effect was associated to a depletion in the concentration of light element near the target surface due to backscattering of the light on the heavy atoms after a single knock-on from the incident ion. As a result, atoms from the light element are emitted from deeper areas in the target, which results in a narrower angular distribution [84]. Such an effect can explain the differences observed in the angular distribution of the metal ratio in the case of HiPIMS, in particular the difference between the light and the heavy elements (see Figure 2b). It should

also be present for MSD, but due to the lower discharge voltage (∼350 V for MSD and ∼600 V for HiPIMS), sputtering is generally less energetic in the case of MSD. Further, due to the rather high pressure-distance product in the current work, effects based on differences in sputtering of the individual elements from the target are only observed in a weakened form, which is particularly true for MSD, where the sputtered particles have less energy than in the case of HiPIMS [57, 85–87]. However, further studies are necessary to explain why the deposition rate in the case of HiPIMS remains constant up to 60° and whether or not it is influenced by the change in chemical composition.

The sudden increase in light elements at 90° deposition angle for both sputter methods can be explained by thermalization (transition from ballistic to thermal flux). Since the major emission flux is directed normal to the target's surface, thermalized ions should be located at higher deposition angle. The increase in light element metal ratio and the decrease in heavy element metal ratio at high deposition angle indicate a more pronounced thermalization, i.e. scattering due to collisions in the plasma cloud of the light element V. The results are in accordance to earlier studies on the influence of thermalized ions on the distribution of heavy elements at higher deposition angles [83].

The most apparent influence of the deposition angle on the films synthesized by CAD is the evolution of the deposition rate with a maximum value at 30°. It is generally accepted in literature that film growth in CAD is proportional to the ion flux, where the latter shows an angular distribution that can be described by a cosine function [88, 89]. Other contributions to film growth in CAD are mainly due to incorporated macroparticles or droplets, a well-known feature of cathodic arc plasmas. However, droplets are typically emitted at angles close to the cathode surface [90], i.e. at angles exceeding 75° in the current work. Further, the synthesized MoNbTaVW films show a relatively low number of incorporated droplets [62] and, hence, the variation in deposition rate cannot be explained by droplets.

The majority of the investigations regarding the angular distribution of the ion flux in arc plasmas was conducted for random cathode spot motion, i.e. without applying a magnetic field. In the current case, a steered arc was used by applying an arched magnetic field in the vicinity of the cathode surface [42]. Meunier and Drouet showed that the ion flux is diverted along the field lines in the presence of a magnetic field [91]. Apparently, the magnetic field component parallel to the cathode surface causes a deflection of the main ion flux from 0 to about 30° deposition angle. Another contribution might be due to the circular erosion zone with a radius of 2-3 cm, where the arc plasma is concentrated in the applied steered arc configuration. However, due to the large distance between cathode and substrate of 25 cm, this influence is of minor importance.

In contrast to the chemical composition of the sputter-deposited films, there is an enhanced concentration of the heavy elements Ta and W along the cathode surface normal, while the fraction of the lightest element V is reduced. Similar results have been reported for the angular distribution of ion fluxes from metal alloy and boride cathodes [92, 93]. In these cases, the ion flux of the heavier elements was more concentrated near the cathode surface normal, i.e. at 0° deposition angle. At intermediate angles the chemical composition is close to the cathode composition, only when approaching 90°, effects based on thermalization as described above for the sputter-deposited films are dominating.

5.2 Thermal stability

This section elucidates the thermal influence on the structure and properties of MoNbTaVW refractory HEA thin films synthesized by CAD. The films were deposited onto Si and Al_2O_3 (0001) single-crystal substrates. Annealing of the as-deposited MoNbTaVW films was performed in a vacuum furnace (HTM Reetz, Germany) from 1000 to 1600 °C in steps of 100 °C and a holding time of 60 min. The pressure of the vacuum furnace rose from 5×10^{-6} Pa to above 6×10^{-2} Pa during annealing between 1000 and 1600 °C.

To assess the film morphology, SEM images of the as-deposited and annealed thin films were taken as depicted in Fig 5.8. These images reveal a smooth thin film surface for the as-deposited film, which remained without significant changes up to an annealing temperature of 1300 °C. While visual observations of the cathodic arc plasma from the MoNbTaVW cathode revealed the emission of droplets due to the high plasma pressure in the cathode spot interacting with molten cathode material, only a limited number of droplets was incorporated into the deposited films. This is similar to previous works [62, 63]. Most likely the vast majority of these droplets reached the growth front of the film in solid state strongly reducing their sticking probability. Starting at 1400 °C, a roughening of the thin film surfaces with the formation of a granular morphology becomes noticeable and increases with increasing annealing temperature. At 1500 °C, partial film delamination occurs and becomes more evident at 1600 °C. A reference annealing at 1500 °C in Ar atmosphere (atmospheric pressure) revealed the same roughening of the film surface but without signs of delamination.

The chemical composition of the films depicted in Figure 5.9 was obtained by EDX. Similarly to the film morphology, the chemical composition of the annealed thin films up to 1300 °C resembled the as-deposited thin film composition. The concentration of the constituting elements in as-deposited state was measured between 18 and 22 at.%, which represents the cathode composition. The concentration of V, the lightest element in the

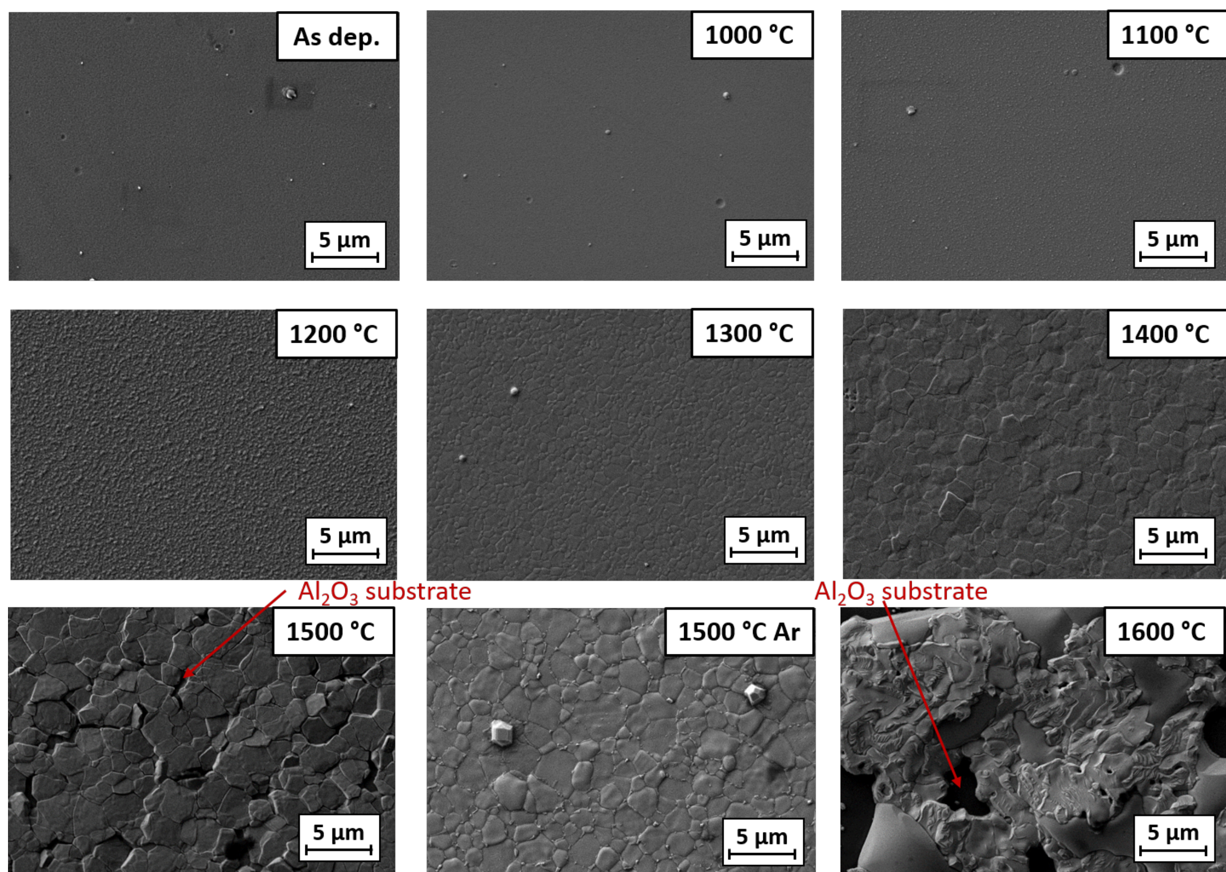

Figure 5.8: SEM top-view images of MoNbTaVW thin films on Al_2O_3 substrates in as-deposited state and after annealing in vacuum and in Ar atmosphere.

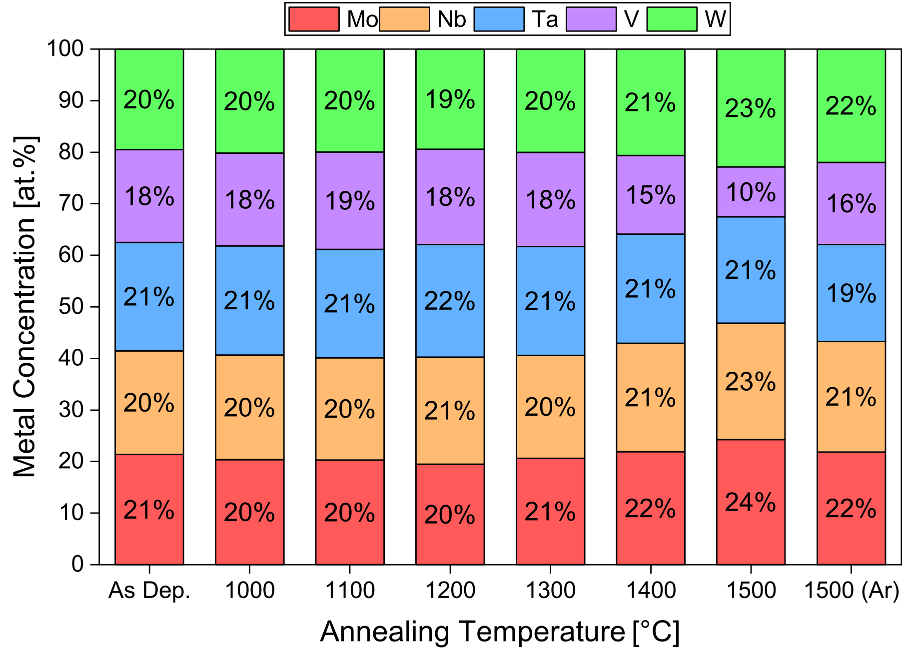

Figure 5.9: Chemical composition of MoNbTaVW thin films on Al_2O_3 substrates in as-deposited state and after annealing in vacuum and in Ar atmosphere. Reference samples annealed at 1500 °C in Ar atmosphere are also shown.

alloy, was measured between 18 and 19 at.% up to 1300 °C. As shown in Figure 5.2, such a reduction in V occurs at an deposition angle of 0 °C for CAD which was the case here [63]. With further increase in annealing temperature at 1400 and 1500 °C, the V content decreases to 10 at.% which is compensated by higher concentrations of Mo, Nb and W. Only the concentration of Ta remains constant at about 21 at.%. The composition of the film annealed at 1600 °C was not measured due to severe film spalling as shown in Figure 5.8. However, the reduction in V content seems to be associated to the vacuum conditions during annealing. The reference annealing in Ar atmosphere revealed a film composition similar to the one in as-deposited state. There are only minor reductions in the V and Ta contents.

To further investigate the reduction of V during vacuum annealing, the vapor pressure for all constituting elements was calculated according to [94, 95] and is shown in Figure 5.10. Sublimation of an element or compound occurs when its vapor pressure is higher than the surrounding pressure at a given temperature. According to the calculations in Figure 5.10, the vapor pressure of V is in the range of the chamber pressure at 1400 °C and above. Hence, the observed reduction in V concentration can be understood by the sublimation of V out of the films during vacuum annealing. It is further comprehensible that the sublimation of V causes the formation of defects in the films, which weakens their adhesion and causes the observed delamination. The latter is confirmed by the SEM images taken from the film

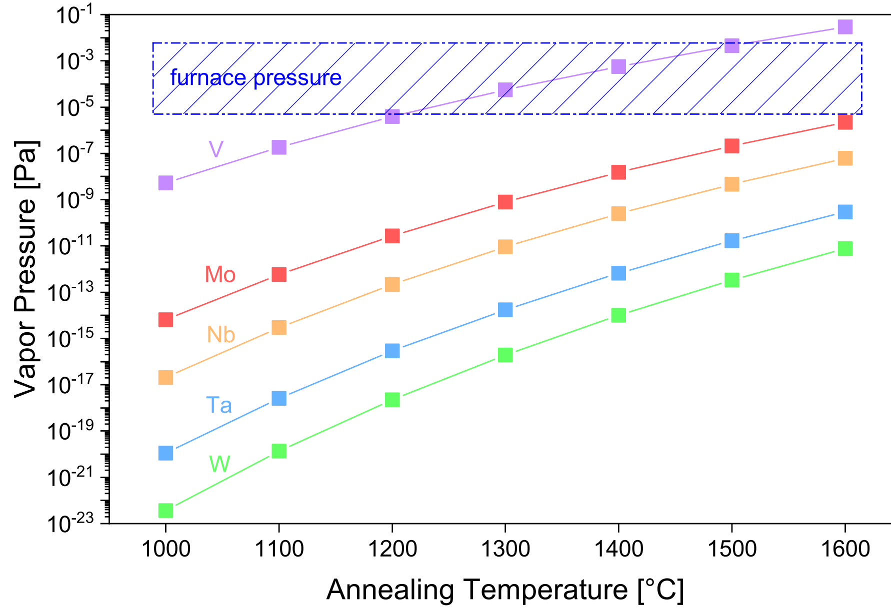

Figure 5.10: Calculated vapor pressure of the constituting elements are depicted according to their respective annealing temperature [94, 95].

annealed at 1500 °C in Ar atmosphere, which showed a roughening of the surface but no delamination (see Figure 5.8).

The film microstructure of the as-deposited and annealed films, as shown in Figure 5.11, was obtained by XRD. The peaks for the as-deposited MoNbTaVW thin film suggest the formation of a single-phase bcc solid solution. The lattice constant a=0.324 nm was calculated from the corresponding (110) peak and is in the range of the thermodynamically stable bcc structures of the different elements present in the film, i.e. a_{Mo}=0.315 nm, a_{Nb}=0.330 nm, a_{Ta}=0.330 nm, a_{V}=0.303 nm and a_{W}=0.316 nm [69]. This is in accordance to the lattice constants calculated in Figure 5.5 [63] and prior publications [40, 62]. However, the calculated lattice constants for the thin films are larger when compared to bulk MoNbTaVW HEA alloys (a=0.318 nm) reported by Senkov et al. [19]. This is most likely due to the formation of defects during film growth and the presence of in-plane compressive stresses of 0.6 GPa in the film (see Figure 5.6) as it is frequently observed for films synthesized by CAD [42]. With increasing annealing temperature first a peak shift towards higher diffraction angles relative to the as-deposited peak position was noticed at 1100 and 1200 °C. At temperatures above, a gradual shift to lower angles can be observed. These peak shifts are most likely related to defect recovery and grain coarsening as frequently observed for films deposited by physical vapor deposition when annealed at temperatures above deposition temperature as it was the case here [96]. The grain coarsening due to annealing is also visible by the increase in intensity and decrease in width of the peaks, in particular the (110) peak. After annealing

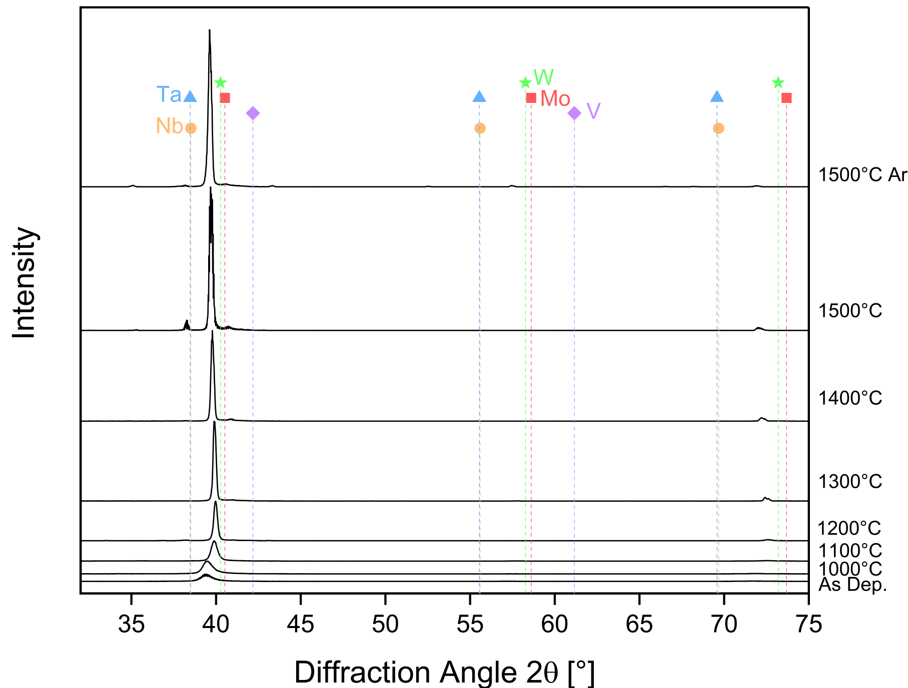

Figure 5.11: XRD diffractograms of MoNbTaVW thin films on Al_2O_3 substrates in as-deposited state and after annealing in vacuum and in Ar atmosphere. Reference peak positions of the thermodynamical stable constituting elements are included [69].

at 1500 °C in vacuum and Ar atmosphere, peaks become visible that could be assigned to elementary bcc phases of Nb and Ta as well as Mo and W. This would indicate the onset of the decomposition of the solid solution, but higher annealing temperatures are necessary to clarify this effect. However, the main peaks recorded at 1500 °C are still clearly associated to the solid solution phase of bcc-MoNbTaVW.

Changes in the electrical resistivity of the as-deposited and annealed thin films were evaluated by four-point probe measurements. Figure 5.12a) shows that the value of the resistivity stays rather constant regardless of the annealing temperature. The minor variations noticeable with increasing temperature are most likely related to defect recovery and grain coarsening [97, 98] as well as to changes in the film morphology due to the sublimation of V. However, the resistivity of the MoNbTaVW HEA thin films is generally by a factor of 2-3 larger than the resistivity of the constituting bulk elements as reported in literature. It is known that defect-rich thin films show a higher resistivity than the respective bulk [99–102]. In the current case, the formation of the solid solution phase comprising all elements might also contribute to the increase in resistivity.

Hardness and Young's modulus of the as-deposited and annealed thin films are depicted in Figure 5.12b). While the Young's modulus remained between 300-350 GPa independent of

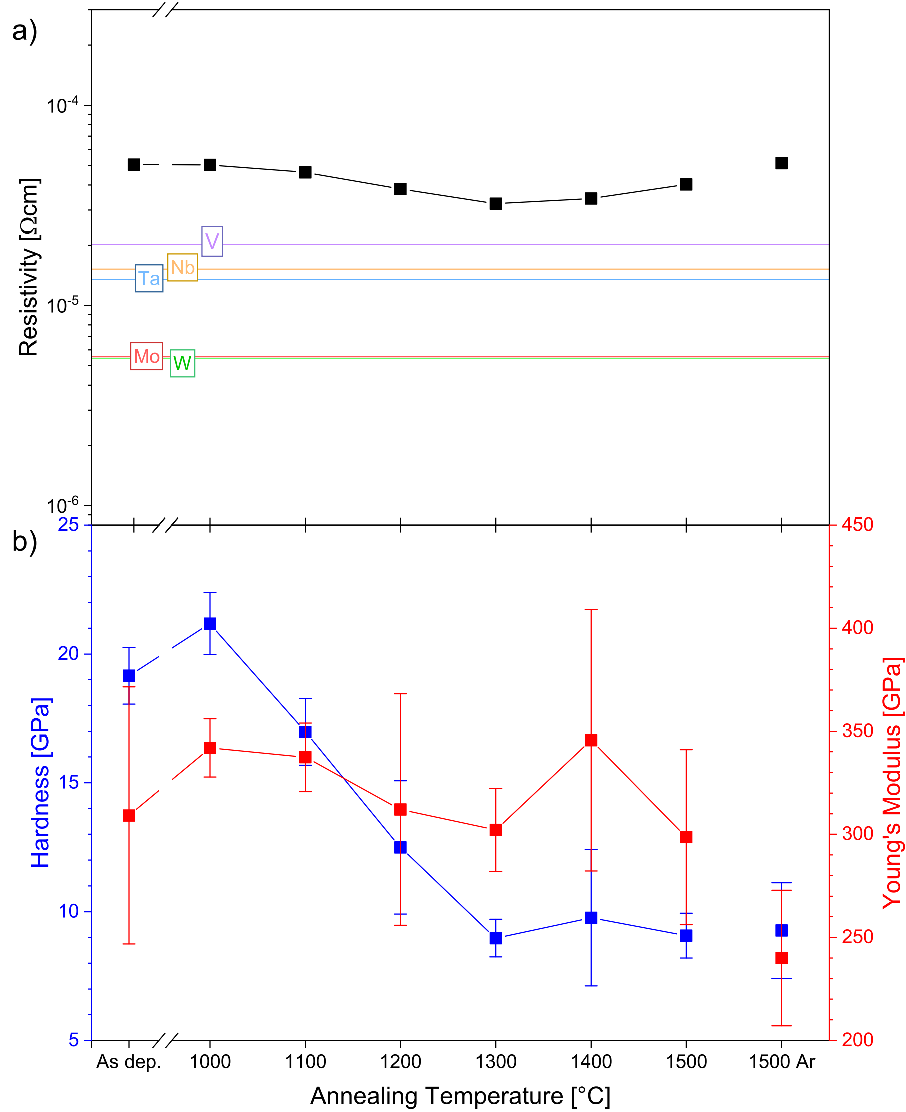

Figure 5.12: Electrical and mechanical properties of MoNbTaVW thin films on Al_2O_3 substrates in as-deposited state and after annealing in vacuum and in Ar atmosphere: a) Electrical resistivity with reference values for bulk metals [103–106] and b) hardness and Young's modulus values.

Table 5.1: Atomic ratio of the metals (mean value and standard deviation) as obtained by WDX averaged over all as-deposited films.

Method	Mo [%]	Nb [%]	Ta [%]	V [%]	W [%]
CAD	21.0±0.3	20.4±0.4	19.5±0.5	18.6±0.6	20.5±0.3
MSD	18.7±0.2	16.5±0.6	19.6±0.3	20.3 ±0.8	24.9±0.6

the annealing temperature in vacuum (the value after annealing in Ar atmosphere is slightly lower), the hardness value decreased with temperature. The value for the as-deposited film is in agreement with the hardness of MoNbTaVW films measured in previous works [62, 63, 107]. However with increasing annealing temperature the hardness value continuously reduced to around 9 GPa after annealing up to 1500 °C. The continuous hardness decrease with increasing annealing temperature is most probably attributed to thermally activated defect annihilation and recrystallization, i.e., decreasing of defect density and stress relaxation [96, 108].

5.3 Effect of N incorporation

This section investigates the effect of N on the microstructure, mechanical and electromechanical properties of refractory $(MoNbTaVW)_{1-x}N_x$ HEA coatings synthesized by CAD and MSD [64].

5.3.1 Chemical composition and structure

As shown in Figure 5.13, with increasing gas flow ratio, the N content in the films increased steadily up to 35 at.% for the CAD films and up to 45 at.% for the ones deposited by MSD. At low gas flow ratios R_{N_2} of up to 5%, the N content in the CAD films was below the detection limit of about 2-3 at.%. However, regardless of R_{N_2}, the atomic ratio of the metals in the $(MoNbTaVW)_{1-x}N_x$ films deposited by CAD was close to equiatomic ratio in the cathode as displayed in Table 5.1. There is only a slight deficiency of V at low values of the gas flow ratio R_{N_2}. A minor deviation from the equiatomic ratio was observed for the films deposited by MSD with a slightly higher W content, mainly compensated by a lower Nb content. Under the given conditions, the metal ratio in the films is not influenced by the nitrogen addition, and seems to originate from a minor deviation in the target composition. XRD diffractograms obtained from the CAD and MSD thin films are displayed in Figure 5.14. Without the addition of N, films deposited by CAD show a (110) diffraction peak resembling the bcc structures of the constituting metal elements. For slightly increasing R_{N_2}

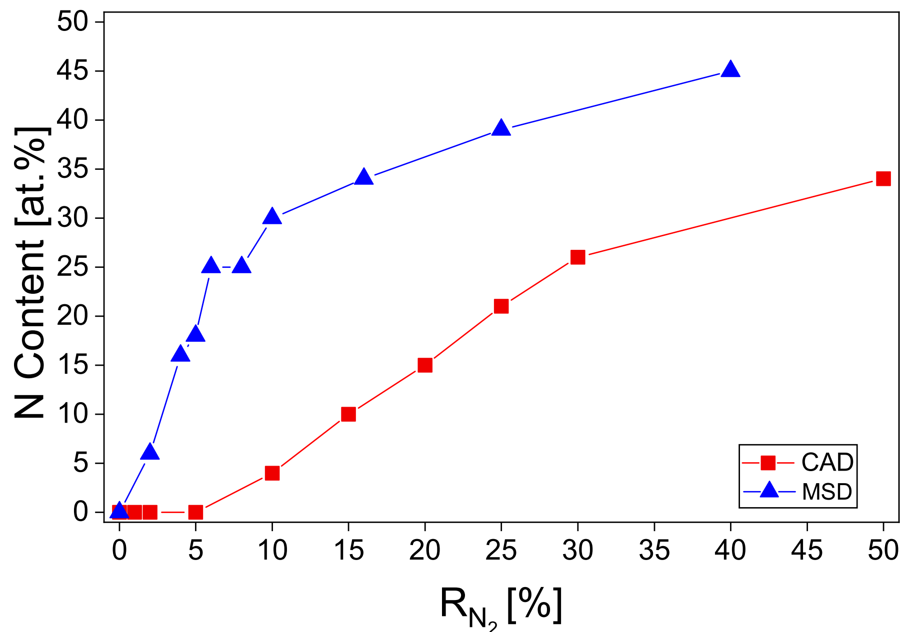

Figure 5.13: N content as measured by WDX for thin films deposited by CAD (red) and MSD (blue) at different gas flow ratio R_{N_2}.

gas flow ratios, up to 5%, a peak shift to lower diffraction angles is noticed. For these films the N content was below the detection limit of the used WDX system. At a N content of 4 at.%, peak broadening is observed.

This trend continues up to 21 at.% of N. In conjunction with the peak broadening also the peak shift starts to reverse. Most pronounced is the peak shift to higher diffraction angles for the film with 21 at.% of N, most likely due to a change in structure. A further increase in the gas flow ratio R_{N_2} resulted in the formation of a fcc phase that can be clearly observed for the film with 35 at.% of N. Similar to the CAD thin films, a bcc crystal structure was also observed for thin films with low N content deposited by MSD. With increasing N content in the films, peak broadening and peak shift towards lower diffraction angles were also present in this case. At N concentrations ranging from 15 to 19 at.% nearly X-ray amorphous films were obtained. With the further increase of the gas flow ratio R_{N_2}, the formation of a fcc phase was observed starting at about 25 at.% of N. At a N content of 34 at.%, the fcc phase can clearly be observed, while at even higher N contents, a change in the preferred out-of-plane orientation can be noticed. Films deposited at the highest nitrogen flows exhibit a random texture, as indicated by the XRD diffractograms.

Further information about the phase transition from bcc to fcc can be obtained from pole figures as demonstrated in previous works [34, 109]. The pole figures depicted in Figure 5.15 were recorded from MSD films and show a similar distinction as the CAD films. For

a film deposited in the low gas flow ratio regime (Figure 5.15a) a clear ring at Ψ=60° was recorded beside the expected central pole. This ring corresponds to the {110} diffraction of the bcc phase, which means that this phase must be present in the sample. It is, however, not visible in the pole figure of the sample deposited in the high gas flow ratio regime (Figure 5.15b) and, hence, a bcc phase is absent in this film.

5.3.2 Electrical and mechanical properties

The electrical resistivity of the deposited films is displayed in Figure 5.16. It rises gradually from about 7×10^{-7} Ωm up to around 4×10^{-6} Ωm with increasing N content in the films regardless of the deposition method. The obtained values for the deposited $(MoNbTaVW)_{1-x}N_x$ films are similar to the resistivity values of the according binary nitride thin films in literature [103–106, 110–114].

Regardless of the N content, the residual stress of the films deposited on silicon was determined between -0.5 and -1.5 GPa for the films synthesized by MSD and between -1 and -2.5 GPa for the arc-deposited films. The hardness is depicted in Figure 5.17. In the case of CAD thin films, a hardness value of 17 GPa was measured for the film without N. With increasing N content up to 4 at.% N an increase in hardness of up to 28 GPa was measured. The hardness remained constant with further incorporation of N up to 35 at.%. At higher N contents, the hardness of the MSD thin films reached values of around 30 GPa, but the increase in hardness was slightly shifted to higher N contents in the thin film as compared to the hardness evolution in the CAD films.

5.3.3 Discussion

Composition and structure

Despite the usage of two different deposition techniques, i.e. CAD with a sintered cathode and MSD with a powder target, the structural properties of the deposited films show noticeable resemblances. Generally, the metal ratio was not influenced by the incorporated N in the thin film, as it remained constant at all gas flow ratios. Hence, the observed changes in structure are solely induced by the incorporation of N and not by variations in the metal ratio as the latter are absent.

With respect to the evolution of the crystallographic structure, a similar trend with increasing N content was indicated in the recorded XRD diffractograms. With the addition of N into the thin film, both deposition methods first yielded bcc metallic MoNbTaVW thin films, which at higher N contents transformed into an X-ray amorphous and eventually a

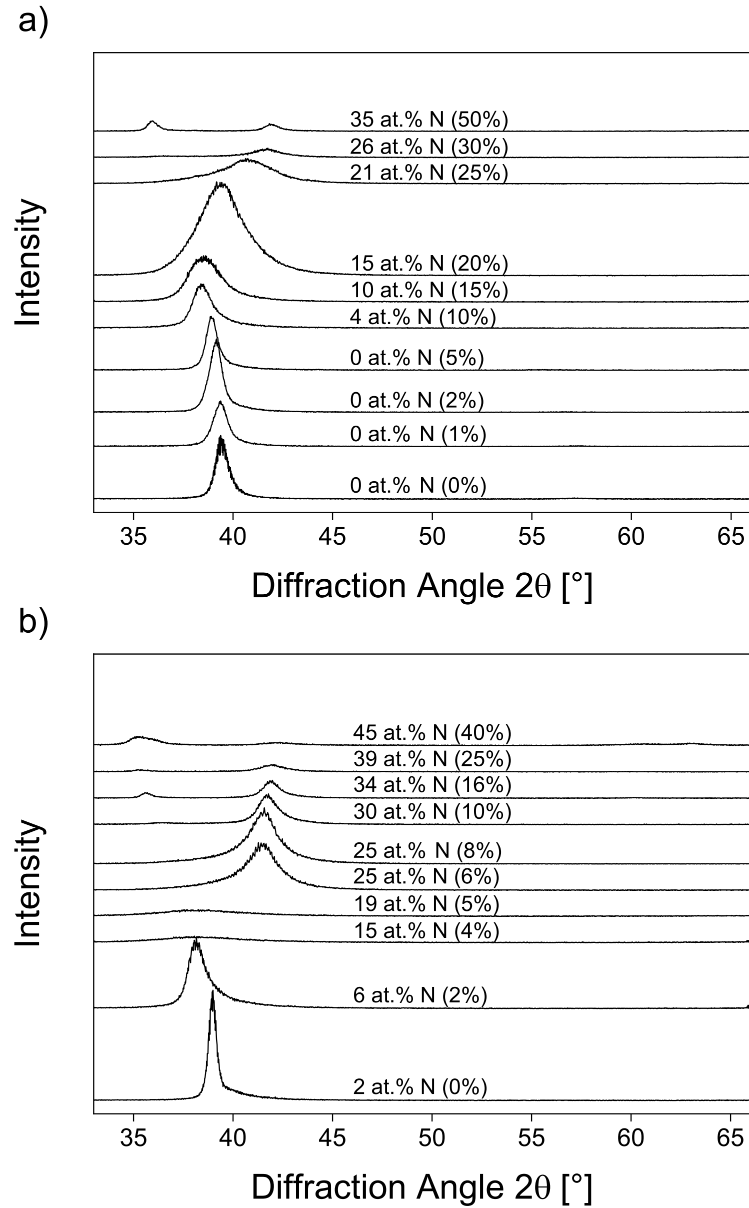

Figure 5.14: XRD diffractograms of as-deposited $(MoNbTaVW)_{1-x}N_x$ thin films synthesized by a) CAD and b) MSD. The diffractograms have been vertically shifted for clarity and the N content is given in at.% while the gas flow ratio, R_{N_2}, is given between parentheses.

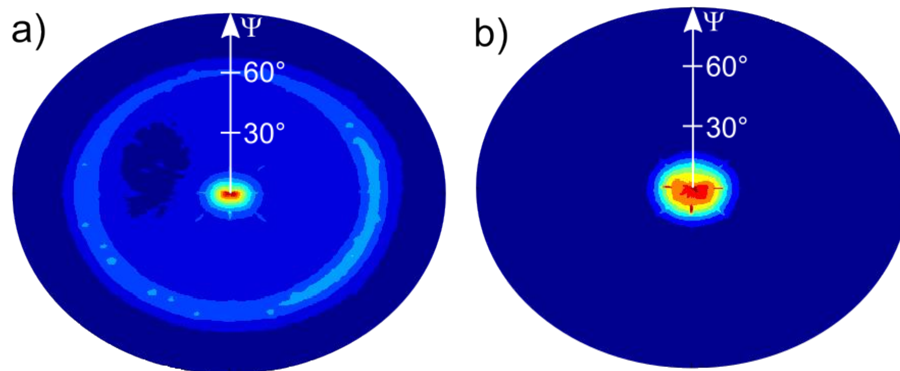

Figure 5.15: a) Typical pole figures for the low gas flow ratio regime (0-6 at.% N) and b) the high flow gas ratio regime (35-40 at.% N).

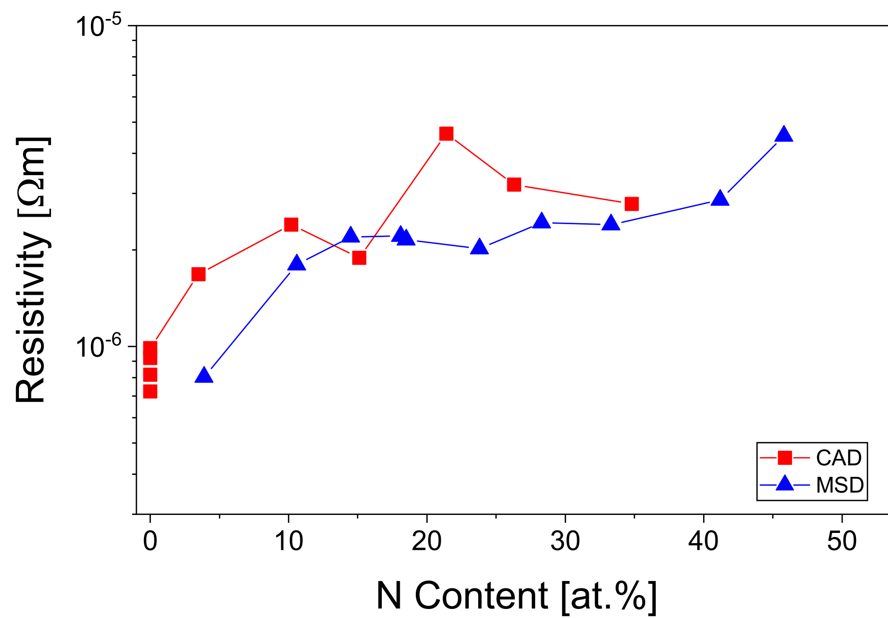

Figure 5.16: Electrical resistivity of synthesized $(MoNbTaVW)_{1-x}N_x$ thin films by CAD and MSD as a function of the N content.

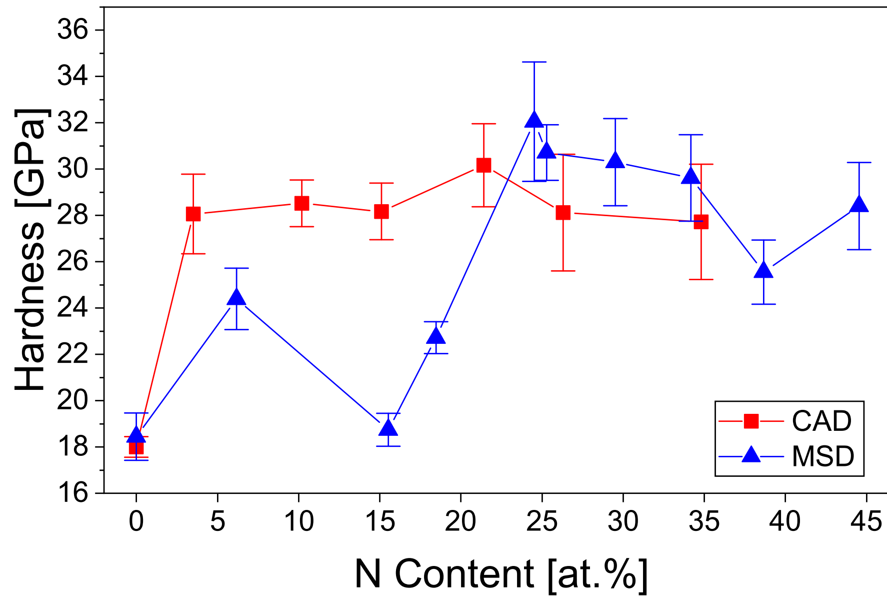

Figure 5.17: Hardness of $(MoNbTaVW)_{1-x}N_x$ thin films synthesized by CAD and MSD.

fcc phase. The phase transition from bcc to fcc with increasing N content was corroborated by the recorded pole figures. At low N content, N atoms are preferentially incorporated at interstitials in the (111) planes, in the case of TiN, HfN, and ZrN [115]. As more N atoms are dissolved into the crystal lattice, lattice distortion either caused by N incorporation induced microstrains or by atomic size mismatch caused by the respective metal atom occurred as evident in the XRD peak shift. The degree of disorder and, hence, the formation of smaller grains is illustrated in the XRD diffractograms, as the peak width increases with increasing N content. Earlier studies conducted by Pelleg et al. found that the expansion of the lattice parameter and hence peak shift is associated with the entrapment of the N or Ar ions during film growth, which is favored at low deposition rates and low temperatures [116]. For MSD in the current work, most likely the peak shift is solely related to N, since lattice expansion is observed with increasing reactive N_2 gas flow and simultaneous decrease in Ar gas flow.

Further addition of N in the thin films ultimately leads to the formation of a fcc nitride solid solution regardless of the deposition method. In the case of CAD, this transition as indicated by the presence of peaks at 41.7° in the diffractogram, which is associated with the fcc phase, appears at a higher gas flow ratio R_{N_2}=30% than for the thin films synthesized by MSD, R_{N_2}=16%. At first sight, the much higher deposition rate, as indicated by the deposition rate in the non-reactive case, during CAD seems an obvious reason. Indeed, the 5 times higher metal flux during CAD as compared to MSD will require more reactive gas to obtain the same stoichiometry. As the higher N_2 partial pressure in CAD yields a higher

N to metal flux ratio as compared to the ratio in MSD, an argumentation based on the deposition rate seems to fail. On the other hand, one needs to account for the enhanced collision probability in the extended plasma as a result of the higher deposition pressure for CAD. Assuming that mainly N atoms or ions originating from the cathode (or target) surface are contributing to the film growth, these N atoms or ions are scattered more severely during the used CAD process and only a reduced flux could be available to be incorporated into the growing film. But as the energies of ions leaving the cathode in CAD are typically higher than the energies of sputtered atoms in MSD [59, 117], it becomes less obvious to use these arguments to explain the higher flow gas ratio needed to form the fcc phase by CAD. A better explanation is based on the interaction of the reactive gas at the cathode or target surface. Poisoning effects are different for both deposition methods [50]. As sputtering is a surface process, the number of sputtered N atoms continuously increases with increasing gas flow ratio R_{N_2} as more and more N atoms and molecules react at the target. Effects of target poisoning during reactive sputtering are well documented [80], and have been demonstrated in the case of HEA [118, 119]. In contrast, material erosion in CAD is a volume process caused by microexplosions in the cathode spots [42]. Even though it is known that the crater size decreases in the presence of a reactive gas like N_2, there is still a significant amount of material that originates from deeper regions in the cathode, not only from the reacted top surface. In addition, nitride (or oxide) layers formed on arc cathodes are typically attractive sites for the ignition of cathode spots preferentially removing such layers, which in turn hinders the incorporation of reactive gases in the modified layer near the cathode surface where all elements present in the cathode are intermixed [120]. In summary, the reason for the necessary higher gas flow ratio R_{N_2}=30% to form the fcc phase by CAD is most likely due to target/cathode poisoning effects.

Properties

The thin film resistivity varied only slightly with the changes in chemical composition and structure and all films exhibited resistivity values resembling metallic conductors (10^{-10} - 10^{-5} Ωm) [105]. A major reason for the apparent higher resistivity values of the metallic films as compared to the resistivity of the elemental bulk metals is due to the scattering size effect at surfaces of the thin film and the grain boundary scattering size effect, predicted by the Fuchs-Sondheimer model [99, 121, 122] and the Mayadas-Shatzkes model [123], respectively. These theories are confirmed by recent publications [124, 125]. Another reason is due to the typically higher defect density in thin films, hindering the charge transport and, hence, resulting in a higher resistivity [50].

The general increase in hardness with increasing N content is due to the phase change from bcc (metallic) to fcc (nitride). Binary nitride phases from transition metals are known to exhibit a high level of hardness, which is one of the reasons for their use as protective and wear-resistant coatings [23]. In the case of CAD, already the incorporation of interstitial N (before the formation of the nitride phase) causes a substantial increase in hardness. This is most likely related to the formation of a crystalline structure. In the case of MSD, there is also an initial increase in hardness (N content of 6 at.%), but with further incorporation of N an amorphous or nearly-amorphous phase forms resulting in a decrease in hardness. Similar hardness values as for the CAD films were obtained for the films with fcc structure or close to the transition point. All these influences lead to a steady hardness increase with increasing N content similar to [126]. Further factors influencing the hardness that need to be considered are the change in crystallite size and the stress state of the films. Apart from the reduction in hardness of the MSD films with N contents between 15 and 20 at.% caused by the formation of an amorphous (or very nanocrystalline) phase, the change in grain size in the films seems to have only a minor impact on the hardness [127, 128]. The change in the width of the recorded XRD peaks in Figure 5.14 indicates a variation in grain size, but films with different crystallite size still show similar hardness values. Furthermore, peak broadening may also be caused by microstrains originating from lattice distortions due to the incorporation of N atoms. However, the influence of the residual stress state in the films seems to be of minor importance as the film stress remained rather constant without a correlation to the changes in chemical composition and structure.

5.4 Electromechanical properties

This section describes the electromechanical behavior of $(MoNbTaVW)_{1\text{-}x}N_x$ thin films, which were deposited on PI by CAD and MSD [63, 64]. The results of metallic MoNbTaVW films are compared to AlCuCrTaTi films synthesized by CAD [63].

5.4.1 Metallic thin films

Figure 5.18 shows the electromechanical behaviour of the films during in-situ uniaxial tensile straining tests. In these experiments the resistance R of each film was recorded during straining and normalized by the resistance of the unstrained film R_0. The critical failure strain was defined as the strain at which the normalized resistance was 10% higher than the theoretical resistance [129]. The MoNbTaVW and AlCuCrTaTi thin films remain intact up

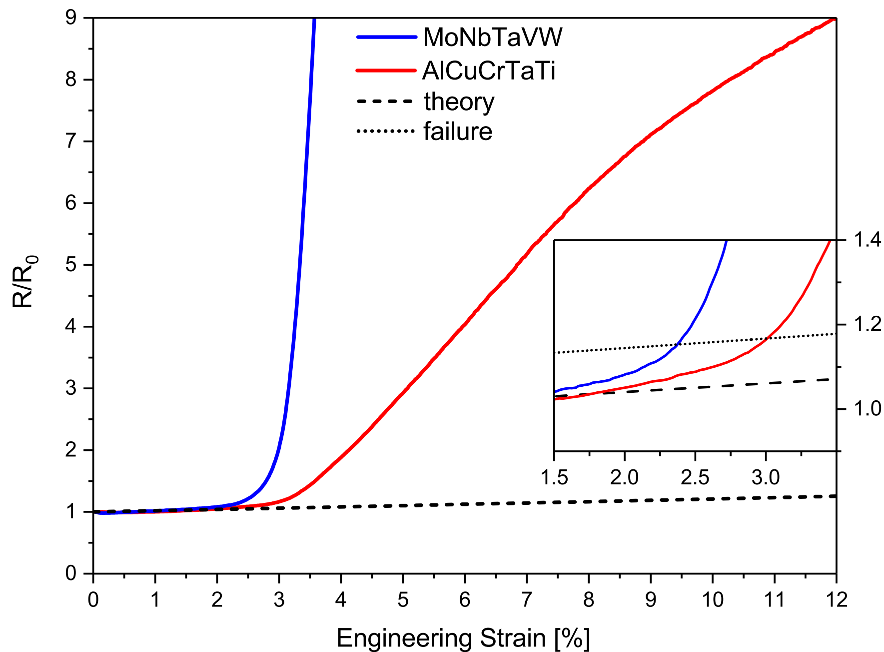

Figure 5.18: Normalized resistance R/R_0 of MoNbTaVW and AlCuCrTaTi thin films as a function of the engineering strain. The dashed line refers to the theoretical prediction [130] and the dotted line indicates the failure criterion.

to 2.3% and 2.9% engineering strain, respectively, with the AlCuCrTaTi curve showing a reduced slope compared to the MoNbTaVW curve.

Images taken during in-situ straining as shown in Figure 5.19 reveal information about crack formation. At a low strain of 0.5% (see Figure 5.19a and d), no defects induced by straining are noticed. The first cracks appear at around 1.8% engineering strain perpendicular to the straining direction. Once the first cracks are formed, their number increases rapidly upon further straining (see Figures 5.19b and e) until it saturates and only widening of the present cracks is observed (see Figures 5.19c and f). The laser intensity images reveal that cracks on both films start to form around growth defects, in particularly at growth defects caused by the incorporation of droplets. As mentioned above, the AlCuCrTaTi film contains more droplets than the MoNbTaVW film due to the differences in the interaction with the arc plasma among the elements present in the cathodes [42]. Furthermore, the images also show that cracks on the MoNbTaVW film are thinner and propagate nearly straight through the entire sample width, while cracks grown on the not uniform AlCuCrTaTi film are shorter, crooked, and more isolated.

Another consequence of the straining is the formation of buckles as a result of the elastic mismatch between film and substrate. On the AlCuCrTaTi film, triangular shaped buckles

form with their basis parallel to the initial crack. The growth of the buckles is limited by their direct neighbouring cracks or when a crack at the apex of the buckle is formed (see Figure 5.22f). In contrast, straight buckles between two neighbouring cracks and parallel to the straining direction are formed on the MoNbTaVW film. On the vast majority of these buckles cracks are formed at the apex causing spalling of the film. This is a result of the brittle nature of the refractory elements present in this HEA thin film [130, 131].

The obtained optical failure strain information was then compared to those values from the electrical measurements in Figure 5.20, where both in-situ crack density and in-situ electrical conductivity values are obtained at specific engineering strains. The average crack density and crack length values were calculated using a line intercept method by counting the number of cracks intersecting three lines across the entire surface image using the software Gwyddion [132]. Crack density saturation for both coatings was identified at around 6% engineering strain with an average crack density of 0.12 cracks/μm (MoNbTaVW) and 0.05 cracks/μm (AlCuCrTaTi). Figure 5.20 also reveals that the increase in film resistance, i.e. deviating from the theoretical line, coincides with the first rise in crack density for both films. Further, the higher saturated crack density of MoNbTaVW than that of AlCuCrTaTi seems to correlate with the more pronounced increase in resistance of MoNbTaVW. However, additional factors need to be considered in understanding the different rises in resistance between both films. In particular, the crack propagation and length of the cracks play a major role. As shown in Figure 5.19c, the MoNbTaVW film mainly revealed straight, elongated and through thickness cracks, which hinder the transport of electrical current in straining direction profoundly and cause a strong rise in resistance. The minimum crack saturation spacing and the initial fracture strain were determined to calculate the interfacial shear stress (IFSS) [133]. The neighbour ratio was considered to verify the validity of the shear [134–136]. The calculated IFSS are 371 MPa for the MoNbTaVW and 154 MPa for the AlCuCrTaTi film. The IFSS value for MoNbTaVW is by the factor of 2 larger than the one for AlCuCrTaTi film as well as the e-beam evaporated pure Cr, Ti and sputter-deposited Mo films on PI according to literature [133, 137, 138]. For example, the calculated IFSS value of a pure Mo film of similar thickness as the analyzed MoNbTaVW film was 130 MPa [138]. This illustrates that alloying of metal films deposited on polymer substrates can increase the IFSS.

5.4.2 Nitride thin films

The representative normalized resistance R/R_0 curves of the $(MoNbTaVW)_{1-x}N_x$ thin films with varying N content during uniaxial straining tests are shown in Figure 5.21. The critical

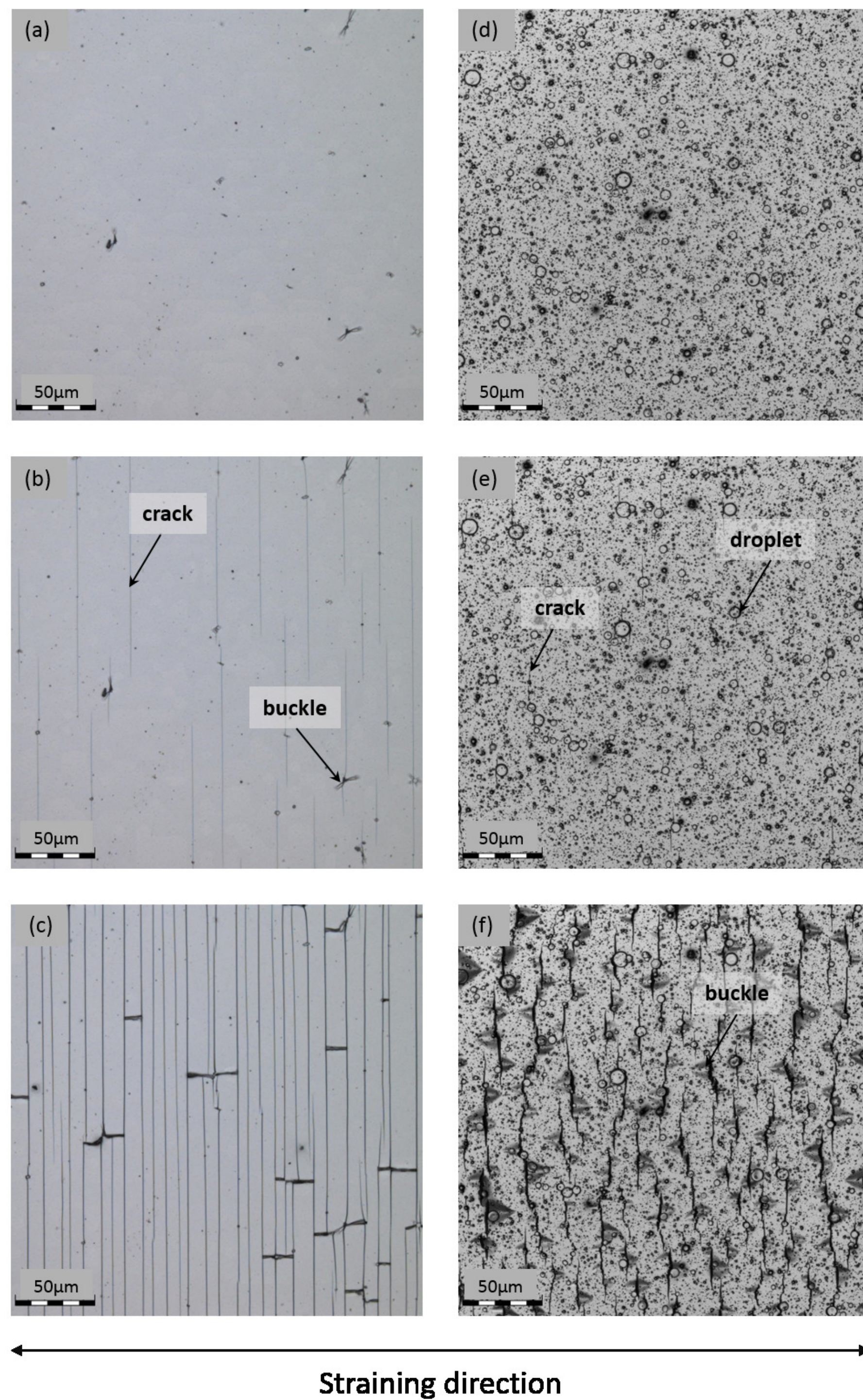

Figure 5.19: Laser scanning micrographs of MoNbTaVW film on PI at a) 0.5%, b) 2.5%, c) 8% engineering strain and AlCuCrTaTi film on PI at d) 0.5%, e) 2.5%, f) 8% engineering strain.

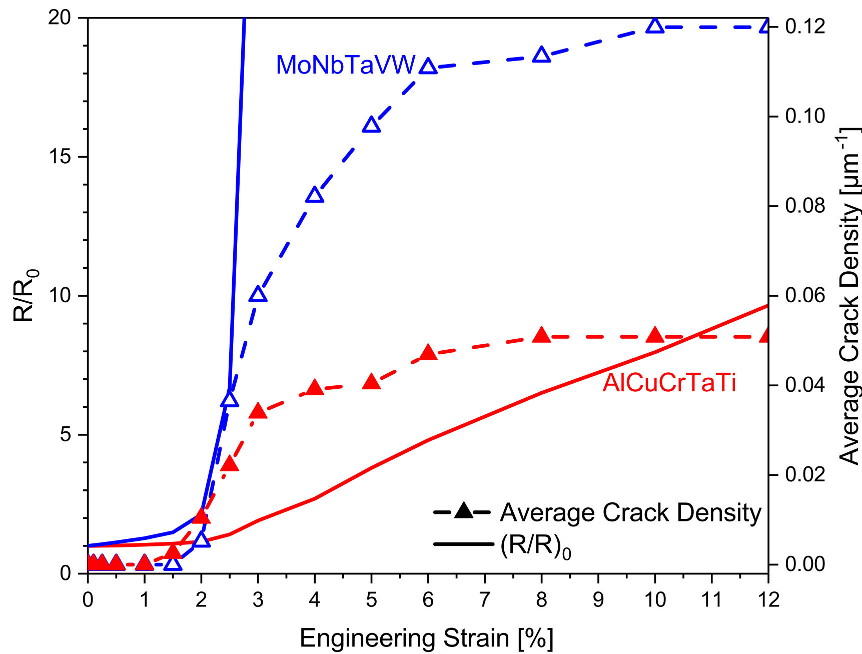

Figure 5.20: Normalized resistance R/R_0 (straight lines) and average crack density (dashed lines) of the MoNbTaVW and AlCuCrTaTi thin films as a function of the engineering strain.

failure strain is defined as the strain at which the normalized resistance was 10% higher than the theoretical resistance obtained from the constant volume approximation [129]. With increasing N content in the CAD deposited films, an earlier rise of the normalized resistance was observed. The film with 0 at.% N failed at 2% engineering strain while the film with 35 at.% N already failed at 0.2%. In the case of the MSD thin films the failure strain for the film without N was reached at 0.8% engineering strain while the films containing 30 and 34 at.% N failed below 0.5%. The failure strain for thin films containing 6 and 39 at.% N was observed at 1.5% and 1.1% engineering strain, respectively.

Further information about the electromechanical behavior of the films, in particular about the formation of cracks, was determined by straining tests with in-situ optical observation using a confocal laser scanning microscope. The in-situ experiments allow the observation of tensile straining induced cracking rather than the residual stress cracking. Here, the crack onset strain (COS) is defined as the strain when the first cracks are observed [136]. Confocal laser scanning micrographs from crack onset and crack saturated films, deposited by CAD and MSD, at their respective engineering strains are depicted in Figure 5.22. Regardless of the deposition method, the micrographs of all films show substrate scratches. These increase the electrical resistance, and thus greatly influence the determination of the

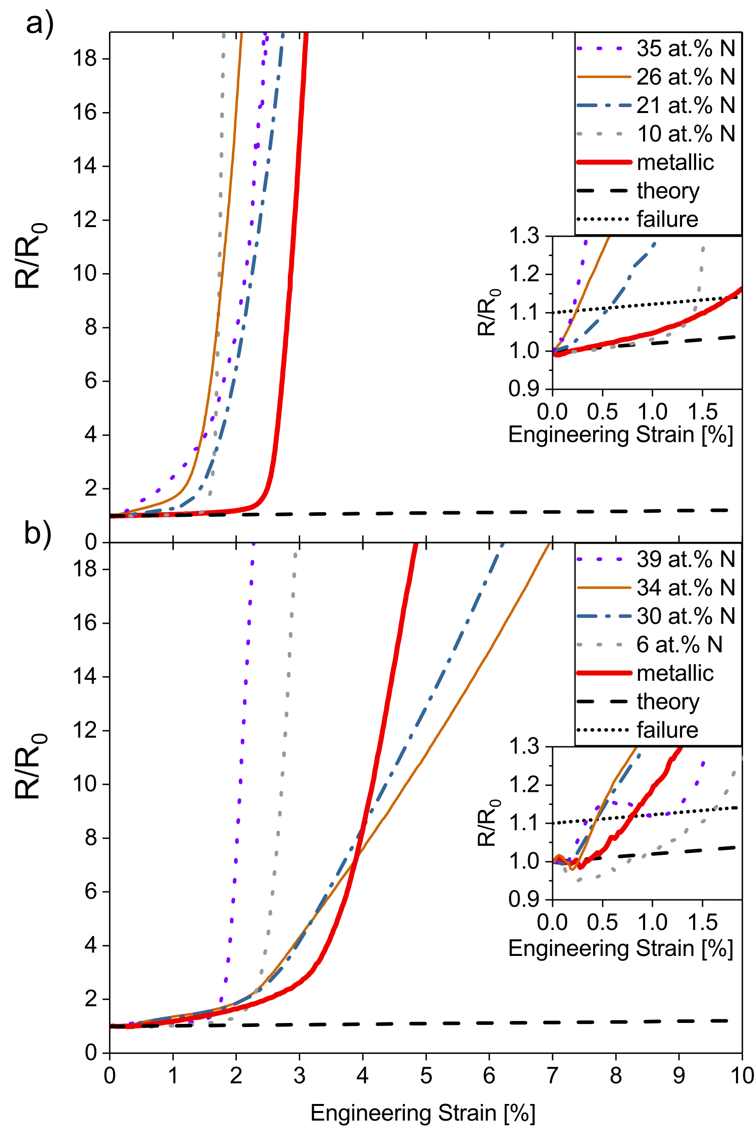

Figure 5.21: Normalized resistance R/R_0 of $(MoNbTaVW)_{1\text{-}x}N_x$ thin films deposited on PI by a) CAD and b) MSD as a function of engineering strain. The dashed black line refers to the theoretical prediction [139], and the dotted black line indicates the failure criterion.

COS by resistance measurements. With increasing N content in the films, cracks in the as-deposited state become evident. After the application of a certain level of engineering strain, straight cracks are formed perpendicular to the straining direction. As a consequence of straining, buckles are formed due to the elastic mismatch between the film and the substrate. The formation of buckles is more pronounced in the case of the films synthesized by CAD.

From the COS on, the observed cracks are counted to calculate the average crack density at their respective engineering strains. The average crack density at each straining step of the thin films deposited by CAD and MSD, as shown in Figure 5.23a and b, respectively, was determined from confocal laser scanning micrographs. Average crack density saturation for the film without N synthesized by CAD was measured at around 6% engineering strain. The point at which the crack saturation is reached shifts towards lower engineering strain for N containing thin films. Thin films containing 26 at.% and 35 at.% N had the highest amount of N within the series and reached the crack saturation at 2% engineering strain. The average crack density after saturation was between 0.1 and 0.16 μm^{-1} for the metallic and the N containing films, which is equal to 10 and 6.3 μm crack spacing (CS). For the thin films with 26 at.% N, the average crack density remained between 0.06 (16.7 μm CS) and 0.08 μm^{-1}(12.5 μm CS). Thin films obtained by MSD generally show indications for crack saturation at around 6% engineering strain for all thin films regardless of the N content. Nonetheless, there is still a slight increase in crack density above 6%. The absolute value of the crack density of the thin films with 0, 29, 34 and 39 at.% N is in the range from 0.11 (9.1 μm CS) to 0.15 μm^{-1} (6.7 μm CS), while it is at about 0.07 μm^{-1} (14.3 μm CS) for the film with 6 at.% N.

5.4.3 Discussion

Overall, the sharp resistance increase indicates that both metallic HEA films show a brittle behaviour [140, 141]. In the case of MoNbTaVW a macroscopically bent (curled) sample caused by large compressive residual stress could be observed, leading to an increase of the initial fracture strain. Similar experiments by Jörg et al. revealed failure strains between 0.2% and 1.3% for sputter deposited Mo thin films with different stress levels [142]. Due to the addition of Cu or Re, the failure strain could be increased up to 2.2% engineering strain [141, 143]. Further, the images also show that cracks on the MoNbTaVW film are thinner and propagate nearly straight through the entire sample width, while cracks grown on the not uniform AlCuCrTaTi film are shorter, crooked and more isolated. In addition to the brittle nature of the MoNbTaVW film, the low density of growth defects favors the

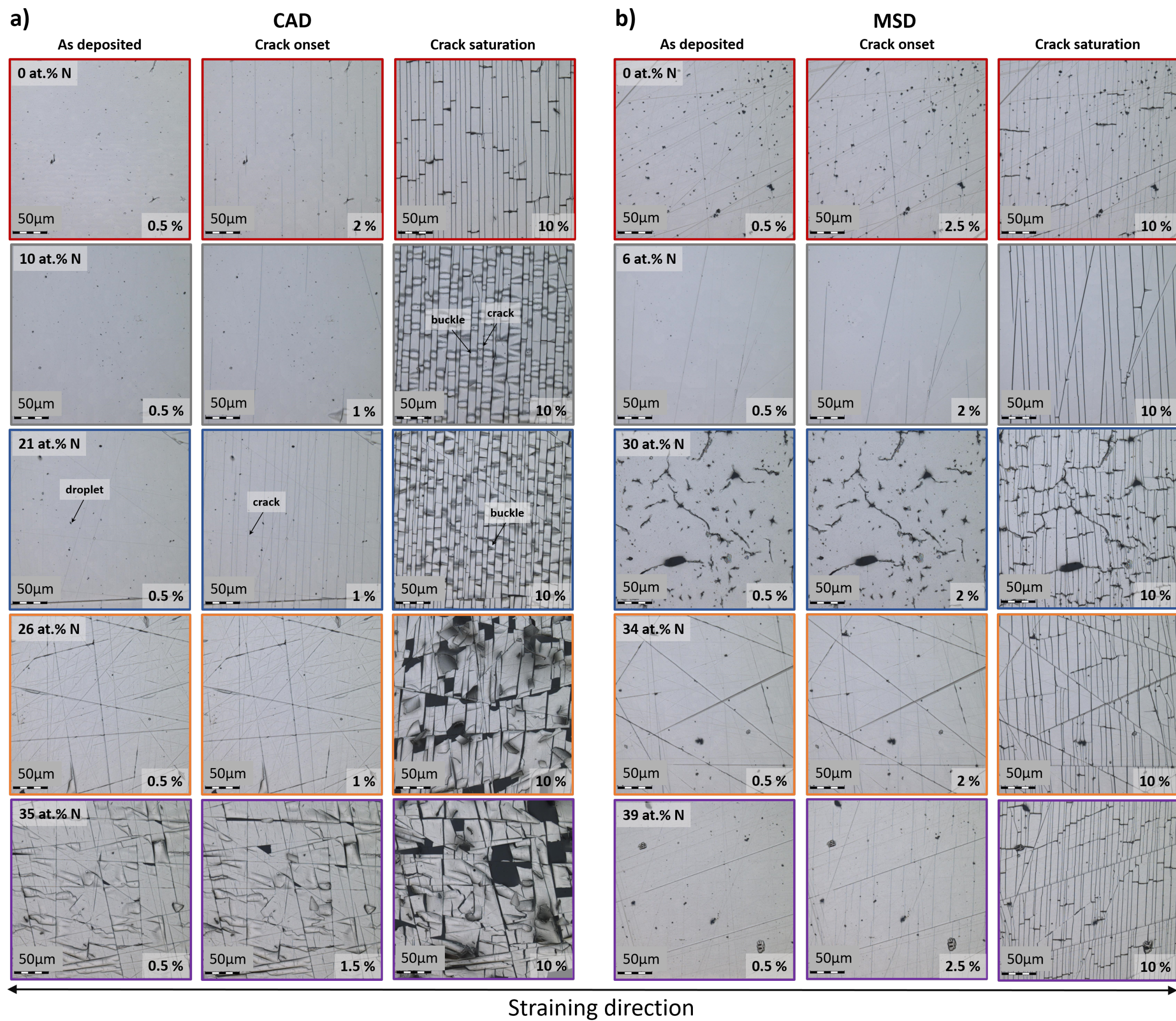

Figure 5.22: Laser scanning micrographs of as deposited, crack onset and crack saturated $(MoNbTaVW)_{1-x}N_x$ film on PI deposited by a) CAD and b) MSD at their respective engineering strains.

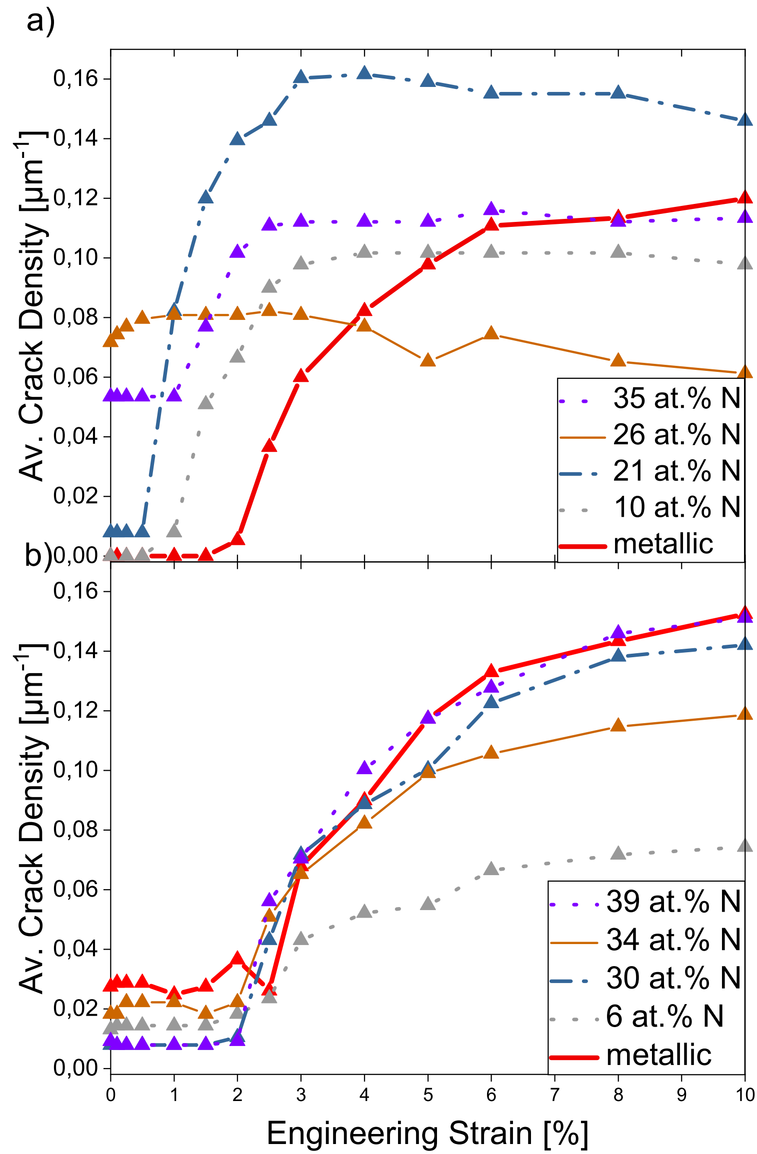

Figure 5.23: Average crack density of $(MoNbTaVW)_{1-x}N_x$ thin films deposited by a) CAD and b) MSD as a function of engineering strain.

formation of elongated cracks. In contrast, the cracks on AlCuCrTaTi are shorter, propagate slower and start to form at growth defects caused by the incorporation of droplets. As the crack length is significantly reduced in the case of AlCuCrTaTi as compared to the crack length on MoNbTaVW, the movement of electrons is less hindered in the more connected AlCuCrTaTi film.

All $(MoNbTaVW)_{1-x}N_x$ thin films show a brittle behavior in the performed tensile tests regardless of N content and deposition method, similar to previous work [62] on metallic films. Failure of the films is on the one hand indicated by the sharp increase in resistance with increasing engineering strain [140] and, on the other hand, by the formation of straight through thickness cracks as observed in [62]. The incorporation of N and the formation of a fcc nitride phase generally results in a further embrittlement. This behavior is more evident for the CAD films, where the COS is lower the higher the N content in the film. With the exception of the film with 6 at.% N, this behavior is also true for the MSD films. In general, the COS obtained from in-situ testing is used as a parameter to provide interfacial shear stresses with the shear lag model estimations for thin films on compliant substrates. The higher the COS, the higher is the film's resistance to cracking under uniaxial tensile loading. Once the COS is reached, a rapid rise in crack density until a saturation level is reached, where no further cracks are formed [140, 141]. Information regarding crack formation during in-situ straining, as shown in Figure 5.23, reveal similar crack saturation values for both deposition methods.

6 Conclusions

Within the current thesis, metallic MoNbTaVW and $(MoNbTaVW)_{1-x}N_x$ HEA thin films were successfully synthesized by different PVD techniques using corresponding composite cathodes. The PVD techniques comprise dc MSD, HiPIMS and CAD. The HEA thin films were synthesized in high vacuum with the addition of Ar and/or N_2. The cathodes were composed of MoNbTaVW in equiatomic ratio. For all HEA thin films, related structure and properties were examined. Following conclusions can be made:

HEA structure

- Regardless of deposition angle and deposition technique, determining the deposition rate and film growth conditions, all MoNbTaVW films formed a solid solution with a bcc structure with only minor changes in the chemical composition.
- The bcc structure of MoNbTaVW HEA thin films is thermally stable up to 1500 °C.
- Higher energetic growth conditions present in HiPIMS and CAD favors the formation of a dense microstructure in the films resulting in higher compressive stress states and hardness values.

Influence of N_2

- The addition of N_2 during deposition leads to the formation of $(MoNbTaVW)_{1-x}N_x$ HEA thin films and a change in the solid solution phase from a bcc to fcc lattice.
- The phase transition appears to be controlled entirely by the metal to N ratio in the film and is therefore independent of the deposition methods indicating a minor influence of the film growth conditions on the structural evolution.

HEA properties

- A hardness value of ~18 GPa was obtained for the metallic MoNbTaVW HEA thin film. Hardness decreases with increasing temperature during vacuum annealing due to thermally activated decreasing of defect density and recrystallization.

- The incorporation of N generally increases the hardness.
- The electrical resistivity of the MoNbTaVW thin film is hardly influenced by annealing or the incorporation of N.
- In general, MoNbTaVW HEA thin films are brittle and the incorporation of N further enhances the brittleness as determined in tensile tests of films deposited on polyimide substrates.

The conducted studies demonstrate that MoNbTaVW HEA thin films synthesized by PVD methods exhibit promising mechanical properties and thermal properties. Furthermore, the findings can aid the synthesis of HEA thin films with optimized structure and properties for desired applications. Due to the vast HEA compositional space in addition to a wide variety of PVD process parameters, this alloy class of refractory HEAs, in particular the studied MoNbTaVW alloy, offers great potential for optimization by tuning the film composition and deposition parameters for future applications.

7 Abbreviations

bcc	Body-centered cubic
CAD	Cathodic arc deposition
CCA	Complex concentrated alloy
COS	Crack onset strain
dc	Direct current
EDX	Energy dispersive X-ray spectroscopy
fcc	Face-centered cubic
FEG-SEM	Field emission gun scanning electron microscopes
hcp	Hexagonal close-packed
HEA	High entropy alloy
HiPIMS	High power impulse magnetron sputtering
HPPMS	High power pulse magnetron sputtering
IFSS	Interfacial shear stress
LPE	Lattice potential energy
MSD	Mangetron sputter deposition
PI	Polyimide
PVD	Physical vapor deposition
RT	Room temperature
SEM	Scanning electron microscopy
WDX	Wavelength-dispersive X-ray spectroscopy
XRD	X-ray diffraction

References

[1] J. E. Greene, Journal of Vacuum Science & Technology A 35 (5) (2017) 05C204.

[2] D. B. Miracle, Nature Communications 10 (1) (2019) 1805.

[3] J.-W. Yeh, S.-K. Chen, S.-J. Lin, J.-Y. Gan, T.-S. Chin, T.-T. Shun, C.-H. Tsau, S.-Y. Chang, Advanced Engineering Materials 6 (5) (2004) 299–303.

[4] B. Cantor, I. Chang, P. Knight, A. Vincent, Materials Science and Engineering: A 375-377 (2004) 213–218.

[5] J.-W. Yeh, Jom 65 (12) (2013) 1759–1771.

[6] B. Cantor, Entropy 16 (9) (2014) 4749–4768.

[7] S.-Y. Chang, C.-E. Li, Y.-C. Huang, H.-F. Hsu, J.-W. Yeh, S.-J. Lin, Scientific Reports 4 (2014) 4162.

[8] S. Sheikh, S. Shafeie, Q. Hu, J. Ahlström, C. Persson, J. Veselý, J. Zýka, U. Klement, S. Guo, Journal of Applied Physics 120 (16) (2016) 164902.

[9] K. Holmberg, A. Matthews, Coatings Tribology: Properties, Mechanisms, Techniques and Applications in Surface Engineering, Elsevier, Amsterdam, Netherlands, 2009.

[10] C. Mitterer, Comprehensive Hard Materials 2 (2014) 449–467.

[11] M. C. Gao, J.-W. Yeh, P. K. Liaw, Y. Zhang (Eds.), High-Entropy Alloys, Springer International Publishing, 2016.

[12] D. B. Miracle, O. N. Senkov, Acta Materialia 122 (2017) 448–511.

[13] B. S. Murty, J. . Yeh, S. Ranganathan, P. Bhattacharjee, High-entropy alloys, Butterworth-Heinemann, Oxford, 2014.

[14] B. Cantor, I. Chang, P. Knight, A. Vincent, Materials Science and Engineering: A 375-377 (2004) 213–218.

[15] J.-W. Yeh, Annales de Chimie Science des Matériaux 31 (6) (2006) 633–648.

[16] J. Chen, X. Zhou, W. Wang, B. Liu, Y. Lv, W. Yang, D. Xu, Y. Liu, Journal of Alloys and Compounds 760 (2018) 15–30.

[17] K.-Y. Tsai, M.-H. Tsai, J.-W. Yeh, Acta Materialia 61 (13) (2013) 4887–4897.

[18] S. Ranganathan, Current Science 85 (10) (2003) 1404–1406.

[19] O. Senkov, G. Wilks, D. Miracle, C. Chuang, P. Liaw, Intermetallics 18 (9) (2010) 1758–1765.

[20] O. N. Senkov, D. B. Miracle, K. J. Chaput, J.-P. Couzinie, Journal of Materials Research 33 (19) (2018) 3092–3128.

[21] O. N. Senkov, G. B. Wilks, J. M. Scott, D. B. Miracle, Intermetallics 19 (5) (2011) 698–706.

[22] M. C. Gao, J.-W. Yeh, P. K. Liaw, Y. Zhang, High-Entropy Alloys Fundamentals and Applications, 2016th Edition, Springer, Cham.

[23] C. Mitterer, PVD and CVD Hard Coatings, in: V.K. Sarin, L. Llanes, D. Mari, C.E. Nebel, Vol. 2, Elsevier Ltd, London, 2014, pp. 449–467.

[24] T. Chen, T. Shun, J. Yeh, M. Wong, Surface and Coatings Technology 188-189 (2004) 193–200.

[25] T. K. Chen, M. S. Wong, T. T. Shun, J. W. Yeh, Surface and Coatings Technology 200 (5-6) (2005) 1361–1365.

[26] C.-H. Lai, S.-J. Lin, J.-W. Yeh, S.-Y. Chang, Surface and Coatings Technology 201 (6) (2006) 3275–3280.

[27] C. Lin, J. Duh, J. Yeh, Surface and Coatings Technology 201 (14) (2007) 6304–6308.

[28] M.-H. Tsai, J.-W. Yeh, J.-Y. Gan, Thin Solid Films 516 (2008) 5527–5530.

[29] W.-J. Shen, M.-H. Tsai, J.-W. Yeh, W.-J. Shen, M.-H. Tsai, J.-W. Yeh, Coatings 5 (3) (2015) 312–325.

[30] V. Dolique, A.-L. Thomann, P. Brault, Y. Tessier, P. Gillon, Materials Chemistry and Physics 117 (1) (2009) 142–147.

[31] V. Dolique, A. L. Thomann, P. Brault, IEEE Transactions on Plasma Science 39 (11 PART 1) (2011) 2478–2479.

[32] B. Braeckman, F. Boydens, H. Hidalgo, P. Dutheil, M. Jullien, A.-L. Thomann, D. Depla, Thin Solid Films 580 (2015) 71–76.

[33] B. Braeckman, F. Misják, G. Radnóczi, D. Depla, Thin Solid Films 616 (2016) 703–710.

[34] R. Dedoncker, P. Djemia, G. Radnóczi, F. Tétard, L. Belliard, G. Abadias, N. Martin, D. Depla, Journal of Alloys and Compounds 769 (2018) 881–888.

[35] R. Dedoncker, G. Radnóczi, G. Abadias, D. Depla, Surface and Coatings Technology 378 (2019) 124362.

[36] K. Yalamanchili, F. Wang, I. Schramm, J. Andersson, M. Johansson Jöesaar, F. Tasnádi, F. Mücklich, N. Ghafoor, M. Odén, Thin Solid Films 636 (2017) 346–352.

[37] O. N. Senkov, G. B. Wilks, J. M. Scott, D. B. Miracle, Intermetallics 19 (5) (2011) 698–706.

[38] P. Malinovskis, S. Fritze, L. Riekehr, L. von Fieandt, J. Cedervall, D. Rehnlund, L. Nyholm, E. Lewin, U. Jansson, Materials & Design 149 (2018) 51–62.

[39] K. Johansson, L. Riekehr, S. Fritze, E. Lewin, Surface and Coatings Technology 349 (2018) 529–539.

[40] Y.-Y. Chen, S.-B. Hung, C.-J. Wang, W.-C. Wei, J.-W. Lee, Surface and Coatings Technology 375 (2019) 854–863.

[41] M. C. Gao, J.-W. Yeh, P. K. Liaw, Y. Zhang (Eds.), High-Entropy Alloys, Springer International Publishing, Cham, 2016.

[42] A. Anders, Cathodic arcs: From Fractal Spots to Energetic Condensation, Springer, New York, 2008.

[43] P. Cools, N. De Geyter, R. Morent, PLA enhanced via plasma technology: a review, in: C. Winthrop (Ed.), New Developments in Polylactic Acid Research, Nova Science Publishers, Inc., 2014, pp. 79–110.

[44] J. T. Gudmundsson, A. Hecimovic, Plasma Sources Science and Technology 26 (12) (2017) 123001.

[45] A. Anders, Thin Solid Films 502 (1-2) (2006) 22–28.

[46] M. J. Druyvesteyn, F. M. Penning, Reviews of Modern Physics 12 (2) (1940) 87–174.

[47] P. M. Martin, Handbook of deposition technologies for films and coatings: Science, Applications and Technology, Elsevier, Amsterdam, 2010.

[48] K. Macák, V. Kouznetsov, J. Schneider, U. Helmersson, I. Petrov, Journal of Vacuum Science & Technology A 18 (4) (2000) 1533–1537.

[49] M. Ohring, Materials Science of Thin Films: Deposition and Structure, 2nd Edition, Academic Press, San Diego, USA, 2002.

[50] D. M. Mattox, Handbook of Physical Vapor Deposition (PVD) Processing: Film Formation, Adhesion, Surface Preparation and Contamination Control, Noyes Publications, Westwood, USA, 2010.

[51] P. Kelly, R. Arnell, Vacuum 56 (3) (2000) 159–172.

[52] W. D. Westwood, Sputter deposition, AVS, New York, 2003.

[53] W. D. Sproul, Surface and Coatings Technology 49 (1-3) (1991) 284–289.

[54] K. Sarakinos, J. Alami, S. Konstantinidis, Surface and Coatings Technology 204 (11) (2010) 1661–1684.

[55] V. Kouznetsov, K. Macák, J. M. Schneider, U. Helmersson, I. Petrov, Surface and Coatings Technology 122 (2-3) (1999) 290–293.

[56] J. Bohlmark, J. Gudmundsson, J. Alami, M. Latteman, U. Helmersson, IEEE Transactions on Plasma Science 33 (2) (2005) 346–347.

[57] V. Kouznetsov, K. Macák, J. M. Schneider, U. Helmersson, I. Petrov, Surface and Coatings Technology 122 (2-3) (1999) 290–293.

[58] U. Helmersson, M. Lattemann, J. Bohlmark, A. P. Ehiasarian, J. T. Gudmundsson, Thin Solid Films 513 (1-2) (2006) 1–24.

[59] A. Anders, Surface and Coatings Technology 257 (2014) 308–325.

[60] I. Petrov, P. Losbichler, D. Bergstrom, J. Greene, W.-D. Münz, T. Hurkmans, T. Trinh, Thin Solid Films 302 (1-2) (1997) 179–192.

[61] D. Karpov, Surface and Coatings Technology 96 (1) (1997) 22–33.

[62] A. Xia, O. Glushko, M. J. Cordill, R. Franz, Journal of Vacuum Science & Technology A 37 (1) (2019) 010601.

[63] A. Xia, A. Togni, S. Hirn, G. Bolelli, L. Lusvarghi, R. Franz, Surface and Coatings Technology (2020) 125356.

[64] A. Xia, R. Dedoncker, O. Glushko, M. J. Cordill, D. Depla, R. Franz, Journal of Alloys and Compounds (under review).

[65] C. Saringer, M. Tkadletz, C. Mitterer, Surface and Coatings Technology 274 (2015) 68–75.

[66] G. G. Stoney, C. A. Parsons, Proceedings of the Royal Society of London. Series A, Containing Papers of a Mathematical and Physical Character 82 (553) (1909) 172–175.

[67] W. D. Nix, Metallurgical Transactions A 20 (11) (1989) 2217–2245.

[68] W. Oliver, G. Pharr, Journal of Materials Research 7 (06) (1992) 1564–1583.

[69] International Centre for Diffraction Data, Card 00-042-1120 for bcc Mo, Card 00-034-0370 for bcc Nb, Card 00-004-0788 for bcc Ta, Card 00-022-1058 for bcc V, Card 00-004-0806 for bcc W, (2017).

[70] L. J. Vandeperre, F. Giuliani, S. J. Lloyd, W. J. Clegg, Acta Materialia 55 (18) (2007) 6307–6315.

[71] B. Bhushan, X. Li, Journal of Materials Research 12 (01) (1997) 54–63.

[72] M. Samuelsson, D. Lundin, J. Jensen, M. A. Raadu, J. T. Gudmundsson, U. Helmersson, Surface and Coatings Technology 205 (2) (2010) 591–596.

[73] J. Emmerlich, S. Mráz, R. Snyders, K. Jiang, J. M. Schneider, Vacuum 82 (8) (2008) 867–870.

[74] A. Anders, Journal of Vacuum Science & Technology A 28 (4) (2010) 783–790.

[75] D. Lundin, K. Sarakinos, Journal of Materials Research 27 (05) (2012) 780–792.

[76] R. R. Olson, M. E. King, G. K. Wehner, Journal of Applied Physics 50 (5) (1979) 3677–3683.

[77] H. H. Andersen, B. Stenum, T. Sørensen, H. J. Whitlow, Nuclear Instruments and Methods in Physics Research Section B 6 (3) (1985) 459–465.

[78] A. Wucher, W. Reuter, Journal of Vacuum Science & Technology A 6 (4) (1988) 2316–2318.

[79] V. S. Tubolt'sev, V. S. Chernysh, V. S. Kulikauskas, Journal of Experimental and Theoretical Physics Letters 63 (7) (1996) 532–536.

[80] D. Depla, S. Mahieu (Eds.), Reactive Sputter Deposition, Vol. 109 of Springer Series in Materials Science, Springer, Berlin, 2008.

[81] D. Horwat, A. Anders, Journal of Physics D: Applied Physics 41 (13) (2008) 135210.

[82] W. P. Leroy, S. Konstantinidis, S. Mahieu, R. Snyders, D. Depla, Journal of Physics D: Applied Physics 44 (11) (2011) 115201.

[83] J. Neidhardt, S. Mráz, J. M. Schneider, E. Strub, W. Bohne, B. Liedke, W. Möller, C. Mitterer, Journal of Applied Physics 104 (6) (2008) 063304.

[84] R. Behrisch, W. Eckstein, Sputtering by Particle Bombardment: Experiments and Computer Calculations from Threshold to MeV Energies, Springer, Berlin, 2007.

[85] I. Petrov, A. Myers, J. E. Greene, J. R. Abelson, Journal of Vacuum Science & Technology A 12 (5) (1994) 2846–2854.

[86] J. E. Greene, Journal of Vacuum Science & Technology A 35 (5) (2017) 05C204.

[87] J. Bohlmark, J. Alami, C. Christou, A. P. Ehiasarian, U. Helmersson, Journal of Vacuum Science & Technology A 23 (1) (2005) 18–22.

[88] B. Jüttner, S. Anders, A. Anders, B. Juttner, Journal of Physics D: Applied Physics 25 (11) (1992) 1591–1599.

[89] H. Fuchs, B. Engers, E. Hettkamp, H. Mecke, J. Schultz, Surface and Coatings Technology 142-144 (2001) 655–660.

[90] J. E. Daalder, Journal of Physics D: Applied Physics 9 (16) (1976) 2379–2395.

[91] J. L. Meunier, M. G. Drouet, IEEE Transactions on Plasma Science 11 (3) (1983) 165–168.

[92] A. G. Nikolaev, E. M. Oks, K. P. Savkin, G. Y. Yushkov, V. P. Frolova, S. A. Barengolts, Journal of Applied Physics 116 (21) (2014) 213303.

[93] A. G. Nikolaev, E. M. Oks, V. P. Frolova, G. Y. Jushkov, Russian Physics Journal 60 (9) (2018) 1528–1532.

[94] T. W. Physik, Institute für Angewandte, Vapor Pressure Calculator, 2020-02-04 (2019). URL `https://www.iap.tuwien.ac.at/www/surface/vapor_pressure`

[95] C. B. Alcock, V. P. Itkin, M. K. Horrigan, Canadian Metallurgical Quarterly 23 (3) (1984) 309–313.

[96] P. Mayrhofer, M. Stoiber, Surface and Coatings Technology 201 (13) (2007) 6148–6153.

[97] P. H. Mayrhofer, A. Hörling, L. Karlsson, J. Sjölen, T. Larsson, C. Mitterer, L. Hultman, Applied Physics Letters 83 (10) (2003) 2049–2051.

[98] A. Knutsson, M. P. Johansson, L. Karlsson, M. Odén, Journal of Applied Physics 108 (4) (2010) 044312.

[99] E. H. Sondheimer, Advances in Physics 1 (1) (1952) 1–42.

[100] D. Dayal, P. Rudolf, P. Wißmann, Thin Solid Films 79 (2) (1981) 193–199.

[101] K.-Y. Chan, T.-Y. Tou, B.-S. Teo, Microelectronics Journal 37 (7) (2006) 608–612.

[102] J. M. Pachlhofer, C. Jachs, R. Franz, E. Franzke, H. Köstenbauer, J. Winkler, C. Mitterer, Vacuum 131 (2016) 246–251.

[103] P. D. Desai, H. M. James, C. Y. Ho, Journal of Physical and Chemical Reference Data 13 (4) (1984) 1097–1130.

[104] P. D. Desai, T. K. Chu, H. M. James, C. Y. Ho, Journal of Physical and Chemical Reference Data 13 (4) (1984) 1069–1096.

[105] S. T. Oyama (Ed.), The Chemistry of Transition Metal Carbides and Nitrides, Springer, Dordrecht, 1996.

[106] M. Fenn, G. Akuetey, P. E. Donovan, Journal of Physics: Condensed Matter 10 (8) (1998) 1707–1720.

[107] S.-B. Hung, C.-J. Wang, Y.-Y. Chen, J.-W. Lee, C.-L. Li, Surface and Coatings Technology 375 (2019) 802–809.

[108] L. Hultman, Vacuum 57 (1) (2000) 1–30.

[109] I. Petrov, P. B. Barna, L. Hultman, J. E. Greene, Journal of Vacuum Science & Technology A 21 (5) (2003) S117–S128.

[110] Y. Wang, J. W. Seok, R. Y. Lin, MRS Proceedings 750 (2002) Y5.11.

[111] R. Sanjinés, M. Benkahoul, C. Sandu, P. Schmid, F. Lévy, Thin Solid Films 494 (1-2) (2006) 190–195.

[112] D. K. Kim, H. Lee, D. Kim, Y. K. Kim, Journal of Crystal Growth 283 (3-4) (2005) 404–408.

[113] J. Zasadzinski, R. Vaglio, G. Rubino, K. E. Gray, M. Russo, Physical Review B 32 (5) (1985) 2929–2934.

[114] S. Anwar, S. Anwar, Surface Engineering 33 (4) (2017) 276–281.

[115] I. Goldfarb, J. Pelleg, L. Zevin, N. Croitoru, Thin Solid Films 200 (1) (1991) 117–127.

[116] J. Pelleg, L. Zevin, S. Lungo, N. Croitoru, Thin Solid Films 197 (1-2) (1991) 117–128.

[117] R. Franz, P. Polcik, A. Anders, Surface and Coatings Technology 272 (2015) 309–321.

[118] P. K. Huang, J. W. Yeh, Surface and Coatings Technology 203 (13) (2009) 1891–1896.

[119] C.-H. Tsau, Y.-H. Chang, Entropy 15 (11) (2013) 5012–5021.

[120] R. Franz, F. Mendez Martin, G. Hawranek, P. Polcik, Journal of Vacuum Science & Technology A: Vacuum, Surfaces, and Films 34 (2) (2016) 021304.

[121] K. Fuchs, Mathematical Proceedings of the Cambridge Philosophical Society 34 (1) (1938) 100–108.

[122] D. K. C. Macdonald, K. . Sarginson, F. E. Simon, Proceedings of the Royal Society of London. Series A. Mathematical and Physical Sciences 203 (1073) (1950) 223–240.

[123] A. F. Mayadas, M. Shatzkes, Physical Review B 1 (4) (1970) 1382–1389.

[124] F. Cougnon, D. Depla, Coatings 9 (5) (2019) 299.

[125] F. G. Cougnon, I. C. Schramm, D. Depla, Thin Solid Films 690 (2019) 137540.

[126] A. Pogrebnjak, V. Beresnev, K. Smyrnova, Y. Kravchenko, P. Zukowski, G. Bondarenko, Materials Letters 211 (2018) 316–318.

[127] P. H. Mayrhofer, Materials Science Aspects of Nanocrystalline PVD Hard Coatings, Ph.D. thesis, Montanuniversitaet Leoben (2001).

[128] Z. B. Qi, P. Sun, F. P. Zhu, Z. C. Wang, D. L. Peng, C. H. Wu, Surface and Coatings Technology 205 (12) (2011) 3692–3697.

[129] Y. Leterrier, L. Médico, F. Demarco, J.-A. Månson, U. Betz, M. Escolà, M. Kharrazi Olsson, F. Atamny, Thin Solid Films 460 (1-2) (2004) 156–166.

[130] O. Glushko, M. Cordill, Experimental Techniques (2014) 303–310.

[131] N. Lu, X. Wang, Z. Suo, J. Vlassak, Applied Physics Letters 91 (22) (2007) 221909.

[132] D. Nečas, P. Klapetek, Open Physics 10 (1) (2012) 181–188.

[133] M. Cordill, A. Taylor, Thin Solid Films 589 (2015) 209–214.

[134] A. Kelly, W. Tyson, Journal of the Mechanics and Physics of Solids 13 (6) (1965) 329–350.

[135] J. Andersons, S. Tarasovs, Y. Leterrier, Thin Solid Films 517 (6) (2009) 2007–2011.

[136] A. Taylor, V. Edlmayr, M. Cordill, G. Dehm, Surface and Coatings Technology 206 (7) (2011) 1830–1836.

[137] M. J. Cordill, A. Taylor, J. Schalko, G. Dehm, Metallurgical and Materials Transactions A 41 (4) (2010) 870–875.

[138] T. Jörg, M. J. Cordill, R. Franz, C. Kirchlechner, D. M. Többens, J. Winkler, C. Mitterer, Materials Science and Engineering: A 697 (2017) 17–23.

[139] O. Glushko, M. Cordill, Experimental Techniques 40 (2016) 303–310.

[140] M. J. Cordill, O. Glushko, B. Putz, Frontiers in Materials 3 (2016) 11.

[141] T. Jörg, D. Music, F. Hauser, M. J. Cordill, R. Franz, H. Köstenbauer, J. Winkler, J. M. Schneider, C. Mitterer, Scientific Reports 7 (1) (2017) 7374.

[142] T. Jörg, M. J. Cordill, R. Franz, O. Glushko, J. Winkler, C. Mitterer, Thin Solid Films 606 (2016) 45–50.

[143] T. Jörg, D. Music, M. J. Cordill, R. Franz, H. Köstenbauer, C. Linke, J. Winkler, J. M. Schneider, C. Mitterer, Applied Physics Letters 111 (13) (2017) 134101.